Determining the feasibility of a real-time geophysical magnetic and electric measurement system for monitoring strain underground

by

Christoph Schaub

A thesis submitted in partial fulfillment
of the requirements for the degree of
Master of Science (MSc) in Geology

The Faculty of Graduate Studies
Laurentian University
Sudbury, Ontario, Canada

THESIS DEFENCE COMMITTEE/COMITÉ DE SOUTENANCE DE THÈSE
Laurentian Université/Université Laurentienne
Faculty of Graduate Studies/Faculté des études supérieures

Title of Thesis Titre de la thèse	Determining the feasibility of a real-time geophysical magnetic and electric measurement system for monitoring strain underground
Name of Candidate Nom du candidat	Schaub, Christoph
Degree Diplôme	Master of Science
Department/Program Département/Programme	Geology
Date of Defence Date de la soutenance	December 10, 2014

APPROVED/APPROUVÉ

Thesis Examiners/Examinateurs de thèse:

Dr. Richard Smith
(Supervisor/Directeur de thèse)

Mr. Damien Duff
(Committee member/Membre du comité)

Mr. Alan King
(Committee member/Membre du comité)

Dr. Christian Dupuis
(External Examiner/Examinateur externe)

Approved for the Faculty of Graduate Studies
Approuvé pour la Faculté des études supérieures
Dr. David Lesbarrères
M. David Lesbarrères
Acting Dean, Faculty of Graduate Studies
Doyen intérimaire, Faculté des études supérieures

ACCESSIBILITY CLAUSE AND PERMISSION TO USE

Abstract

In deep mining environments, rockbursts can occur in areas of high stress. The unpredictable nature, and sometimes fatal consequences of the rockbursts, makes identifying increases in stress that occur prior to failure events, important for mine safety. The piezoelectric, electrokinetic, and seismo-electric/magnetic effects result in rocks that are stressed emitting electric and magnetic fields that can potentially be measured in (or close to) a rock mass. Electric, magnetic and seismic data were collected during a four-day period at Coleman Mine, Sudbury, Ontario, and later analysed. No signals due to strain were evident in the magnetic or electric data, so a more careful three-part experiment was proposed to see if strain related signals could be identified in magnetic data. In the first part of the experiment thirty-two rocks were stressed until failure. Measurable magnetic signals associated with audible cracking sounds were found for most rock samples, as well as consistent signals across all samples prior to failure. The implementation of real-time monitoring of these signals has the potential to significantly improve deep mine safety by mapping the evolution of strain underground and potentially indicating areas susceptible to failure.

Keywords

Stress, Strain, Electric, Magnetic, Real-Time, Underground, Monitoring, Geophysics

Acknowledgments

During my two years at Laurentian University I have been very fortunate to be surrounded by people willing to contribute in a positive way to my research and development as a person, and a geoscientist.

First and foremost, my supervisor, Dr. Richard Smith, who not only gave me the opportunity to make the transition into geophysics, but whos continuous support and mentorship made this period of my life and studies exciting and rewarding. The opportunities that I have been afforded throughout my studies and now after their conclusion are directly related to his passion and enthusiasm to see each of his students succeed.

Thank you to Mr. Alan King, and Mr. Damien Duff, my thesis committee members, for their input, advice, corrections and support throughout my research. I would also like to extend a big thank you to my external examiner, Dr. Christian Dupuis, for his many insightful comments, and helpful corrections to this document. Thank you also to Ben Polser (Vale), and Salina Yong (MIRARCO) for their valuable input concerning my research, experimental design, and the lending of their geophysical equipment.

Thank you to the Centre for Excellence in Mining Innovation (CEMI) and the sponsors of the Smart Underground Monitoring and Integrated Technologies for Deep Mining (SUMIT) project, The Government of Ontario, Vale, Rio Tinto, and Sudbury Integrated Nickel Operations A Glencore Company, for providing financial support.

Finally, I would like to acknowledge the support of my family and friends that have always encouraged me to pursue my dreams. I hesitate to mention names, as there are just too many, and I fear forgetting someone special. In particular I would like to thank my friends in the geophysics office, and our honorary geophysicist in the geology department, for bringing laughs,

memories, ideas, support, and most importantly, friendships that will last a lifetime. To finish, I would like to thank my parents, Gabi and Fred, and my brother, Sam, for being there for me throughout the multitude of highs and lows in every way a son and brother could hope for. For them, this document started 28 years ago.

Table of Contents

List of Tables

List of Figures

1 Introduction

In deep mine environments, areas of high stress can be subject to rockbursts. The occurrence of these rockbursts can be unpredictable and sometimes have fatal consequences, so identifying the strain changes associated with rockbursts is important for mine safety. Geophysical monitoring techniques may be the most plausible method to accomplish this because after initial underground set-up real-time monitoring can be completed from surface. Frid (2001) and Xu et al. (2012) discuss the applications of geophysical monitoring for rockburst forecasting.

It has been shown experimentally (Hui-lin et al. 2009; Xu et al. 2012) that failure phenomena due to high stress in rocks can be measured using geophysical techniques. Acoustic emissions (AE), and seismic wave (SW) monitoring are well documented for forecasting of earthquakes, volcanoes, and more recently in some mines (McNutt, 1996; Mendecki et al., 1999; Crampin, 2001; Werner-Allen et al., 2005). Although the potential for identifying high strain areas in mines is not yet common, there is potential to implement such a system. Recently, electromagnetic emission (EME) have been considered in addition to AE and SW monitoring as laboratory and in field testing has clearly shown correlations between EME, AE, and SW (Kepic, 1995; Kepic et al., 2001; Johnston, 2002; Freund, 2002; Xuequi et al., 2012). Presently EME mainly considers varying electric field and direct electrical current measurements and the exact effects generating the signals are unknown. Magnetic measurements, although rarely discussed in the literature, and untested beyond a few experiments, may also hold some potential for identifying stressed zones. The feasibility of implementing a real time electric and magnetic measurement system to monitor strain in mining environments will be examined.

The majority of methods used for identifying, and mitigating risk in areas susceptible to rock instabilities are mechanical methods, such as de-stress blasting (Sedlak, 1997), water infusion

control (Frid, 2000), spray-on liners (Archibald and Dirige, 2006), cablebolts (Hutchinson and Diederichs, 1996) and overcoring (Sjöberg, 2003). The implementation of these techniques requires a significant investment of resources. Enhanced stress or strain monitoring would increase the overall safety of the mine working environment by allowing the investment to be focussed on the high risk (high stress, high strain areas) (Wang et al., 2005).

Geophysical forecasting of earthquakes has been around for more than half a century (Johnston, 2002) and was really brought into the spotlight in 2009 in L'Aquila, Italy where scientists were later convicted of manslaughter (now acquitted) for failing to give proper notice of a seismic event of magnitude 5.9 on the Richter scale of which they had precursory evidence.

Forecasting of such catastrophic events can be difficult. Early research pertaining to stress release in earthquakes revolved around the light emissions observed by bystanders (Brady and Rowell, 1986), and abnormal animal behaviour attributed to EME signals (Ikeya et al., 2000). The Loma Prieta earthquake (Richter magnitude 7.1) of October 18, 1989 (Smith et al., 1990; Fenoglio et al., 1995) and various earthquakes in Japan (Gokhberg and Morgounov, 1982) resulted in research to monitor stress. The studies carried out in conjunction with the Loma Prieta earthquake, and seismic events in Japan, focused on magnetic measurements taken around the epicenter prior to, and during the events. The signals produced were attributed to electrokinetic and piezoelectric effects, as a result of the generation of strain and fractures in the rockmass, and fluid flow in these fractures.

The majority of modern research regarding earthquakes focuses on movement in stressed rock as an earthquake precursor (Freund et al., 2006), variations in electric potential during slip failure as a result of earthquakes (Yoshida et al., 1997), and EME from microfracturing in a rockmass, due to the high stresses experienced during earthquakes (Molchanov and Hayakawa, 1998). Some

similar monitoring strategies could be applied to forecasting areas of high stress or areas susceptible to failure in mines.

However, very few measurements have been completed in hardrock mines or analogous infrastructure. Lichtenberger (2006) described measurements in the abandoned Wald-Michelbach train tunnel located in the Odenwald Mountains (Germany), far from the nearest city, and from most electromagnetic noise, that shows the potential for measuring stress-related responses using a Cerescope (Greiling & Obermeyer, 2010; Krumbholz, 2010). The electromagnetic moments down the length of the tunnel were measured and correlated with the regional stress field. Additionally, electric and magnetic measurements collected in the Lynx mine, in Victoria (Canada), taken during blasting, show the potential for measuring fields associated with stress in mine environments (Kepic, 1995; Kepic et al. 2001). And finally, multiple quarry blasts carried out in two Brisbane gravel quarries found EME measurements correlated with acoustic and blasting at a distance of 60 m from the blasting site (O'Keefe and Thiel, 1991).

It has been largely shown that EME activity, measured with antennas, increases with stress in underground and open pit coal mines in China (Xuequi et al., 2012). Hui-lin et al. (2009) monitored EME during loading coal from the Muchengjian Coal Mine in the laboratory, and then later correlated the laboratory signals to those emitted underground, concluding that changes in the number, frequency, and amplitude of the signals varies with pressure. Hui-lin et al. (2009) also discovered that pressure increases in the mine, and the associated production of minor cracks in the coal, was related to the appearance, and increases, in the number, and magnitude of EME signals; further increases in pressure and cracking correlated with stronger EME, and upon the release of pressure, the EME strength decreases.

A similar study was carried out by Xu et al. (2012) on the Xingfu Mine located in the center of the Fuxin coal field. The mine had experienced up to 50 rockburst events since the year 2000. Fuzzy logic mathematics was applied to determine the number and amplitude of EME pulses to assess rockburst and failure danger levels in the days preceding a rockburst event, which allowed the mine to take measures towards implementation of preventative measures in areas deemed susceptible to failure. Similar studies for calculating threshold criterion for determining rockburst hazard assessment and monitoring have been completed for different mines by Frid (2001), Lin-Ming et al. (2009), and Dazhao et al. (2010). The majority of the examples also include AE and SW in their monitoring systems. Xuequi et al. (2012) give a very complete summary on the status of using EME to locate zones of potential coal and rock failure. In their discussions they cover the characteristics of EME caused by rock and coal under stress; the correlations between EME and high stress and failure; the memory effect in areas of previously stressed rock; changing stress regimes, and finally the development of criteria for early warning systems. This information has been used to implement thresholds and safety rating systems dependent on the number and amplitude of EME pre-courser events prior to rockbursting and failure in some mines such as the Xingfu Mine.

Although a lot work has already been completed towards developing a continuous monitoring system to measure and quantify the signals emitted due to the effects of stress in underground and above ground workings for fully operational mines, significantly more must be accomplished before such systems can be fully implemented and relied upon. Under CEMI's (Center for Excellence in Mining Innovation) SUMIT (Smart Underground Monitoring and Integrated Technologies for Deep Mining) Project 3B, geophysical data were collected for the purpose of real-time monitoring in deep mines. The data collected were magnetic, microseismic,

direct current induced polarisation (DCIP), gravity, pressure, and temperature; the location was the Coleman Mine in Sudbury Ontario, and the data were collected between July 3rd and July 6th 2014 (Pun 2011). An overview and initial analysis of the data was completed by Pun (2011), in an attempt to identify any strain related signals in the aforementioned data sets. As part of this thesis, further investigation was carried out in an attempt to identify signals related to strain in the electric and magnetic data sets. These results are presented in Section 3.1.

Although no signals directly correlated to strain related events were observed, the analysis provided an indication that examining multiple geophysical data-sets could be effective. A multi-part experiment was developed from the lessons learned from the results and data collection techniques. The first part of which was an above ground magnetic test carried out on April 26th, 2014, the results of which can be found in Section 3.2. The above ground experiment determined the feasibility of measuring magnetic signals when a rock was stressed by an air driven system. As minimal work had been completed on measuring these magnetic responses previously, and the mechanism behind the signal generation is still under debate, the goal of the experiment was to set a preliminary baseline from which subsequent tests could be designed to identify signals due to stressed/strained rock. The above ground magnetic test could be followed up with further above ground testing to provide information on the effects of seismic motion on the magnetic measurement equipment. And finally, a carefully controlled, passive acquisition, underground test could be carried out in a deep mine location. Successful identification of signals due to strain could potentially prove the feasibility of a real-time underground geophysical monitoring system to improve safety in a hardrock mine.

2 Theory

Strained rocks undergo atomic-level processes that produce electric fields due to polarisation of the crystal structure. If the conductivity of a rock is non-zero, the electric field generates currents with associated magnetic fields. And as these magnetic fields vary as a function of time, subsequent electric fields are induced. Depending on the frequency of the fields and the conductivity of the environment, these fields can propagate or diffuse through the rock. These fields, shown in Figure 1, could conceivably be measured using electric and/or magnetic field sensors.

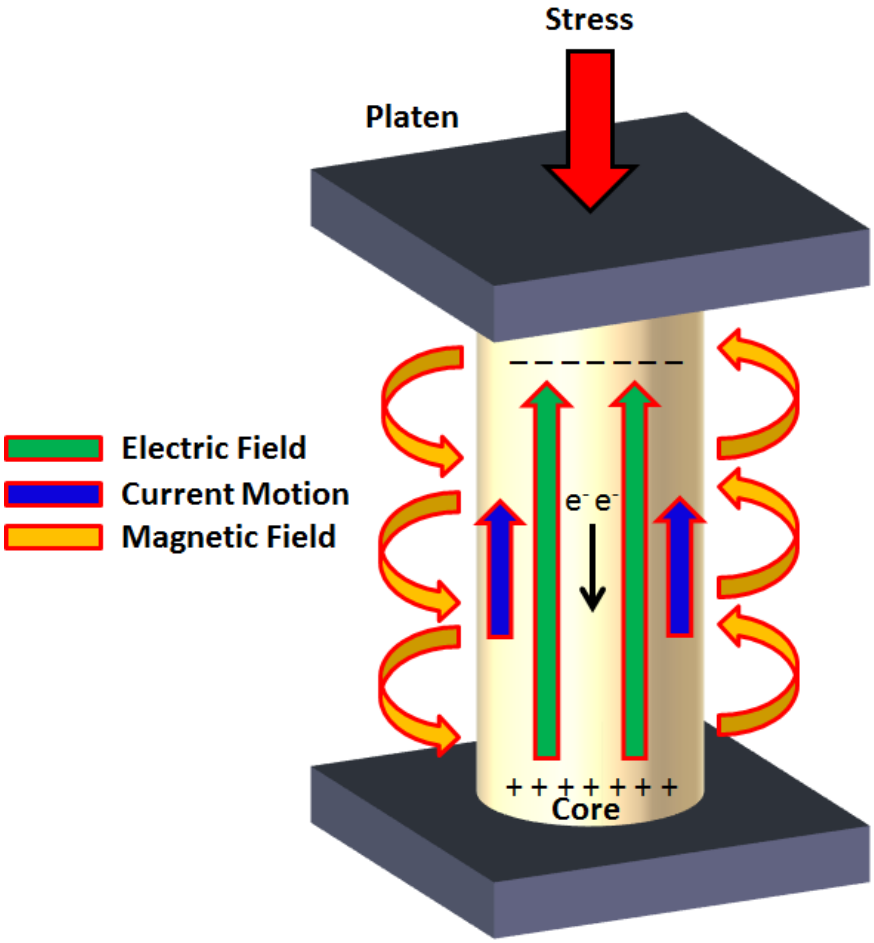

Figure 1. Strained rocks undergo atomic-level processes that produce electric fields due to polarization of the rock mass. The charge movement due to the polarization can

create conventional currents due to charge movement through the lattice (Freund 2002; Freund et al., 2006), and electric fields in the opposite direction to this electron flow. These currents have associated magnetic fields, and as these magnetic fields vary as a function of time, further electric fields are induced.

Nitsan (1977) was one of the first to attribute EME to fracturing rock while studying the piezoelectric response in rock under stress, comparing signals from piezoelectric quartz-bearing rocks, to those containing non-piezoelectric constituents. Subsequent workers have generated multiple mechanisms for explaining how, electric and magnetic emission is stimulated in rock under stress. Although no one theory is yet universally accepted the most commonly found in the literature include (Figure 2), the piezoelectric effect (Nitsan, 1977; Yoshida & Ogawa, 2004), and electrokinetic effects from streaming potentials, and seismo-electric/magnetic effects (Mizutani et al., 1976; Yoshida et al., 1998; Freund, 2002; Takeuchi et al., 2005; Dupuis, 2008), which can generate currents, electric, and magnetic fields that can be measured in a laboratory environment (Goldbaum et al., 2003; Frid et al., 2003; Triantis et al., 2008; Vallianatos & Triantis, 2008; Mori et al., 2009; Carpinteri et al., 2012). When piezoelectric minerals, such as quartz, undergo mechanical stress, a redistribution of charge can create a polarisation in the rock mass. Free charge within the rock mass will adjust to minimise the polarisation, and this redistribution of charge will have associated electric and magnetic fields (Wan et al., 2008). The electrokinetic effects are due to an electric double layer between an electrolyte in pores and fractures, and the surrounding solid grain boundary. The electrolytic fluid will undergo charge re-distribution more rapidly than the grains surrounding the fluid. Streaming potentials result in electric fields due to fluid flow in the rock mass from volume changes, faulting, and fracturing as a result of the electrokinetic effect from stress (Gershenzon et al., 2014). The seismo-

electric/magnetic effect results from the movement of electrolytic ions, and the subsequent generation of electric currents, due to p-wave propagation in the electrolyte (Freund, 2002; Zhu, 2008; Bordes, 2008). The magnitude and contribution to electric and magnetic signals of each of these effects are still somewhat unknown. These are the most commonly discussed effects for the generation of measurable fields from strained rocks.

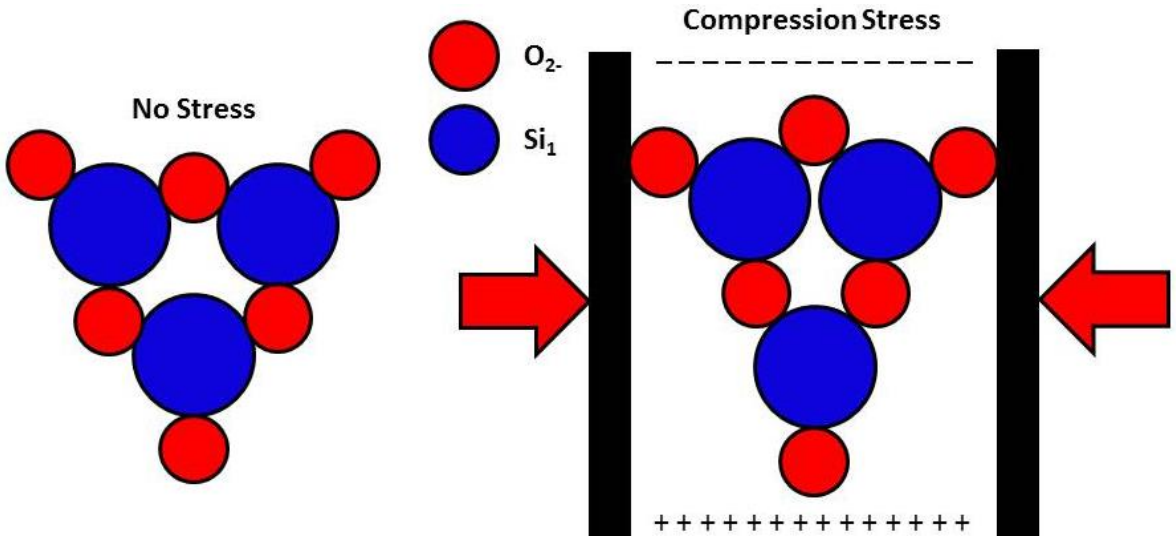

(a)

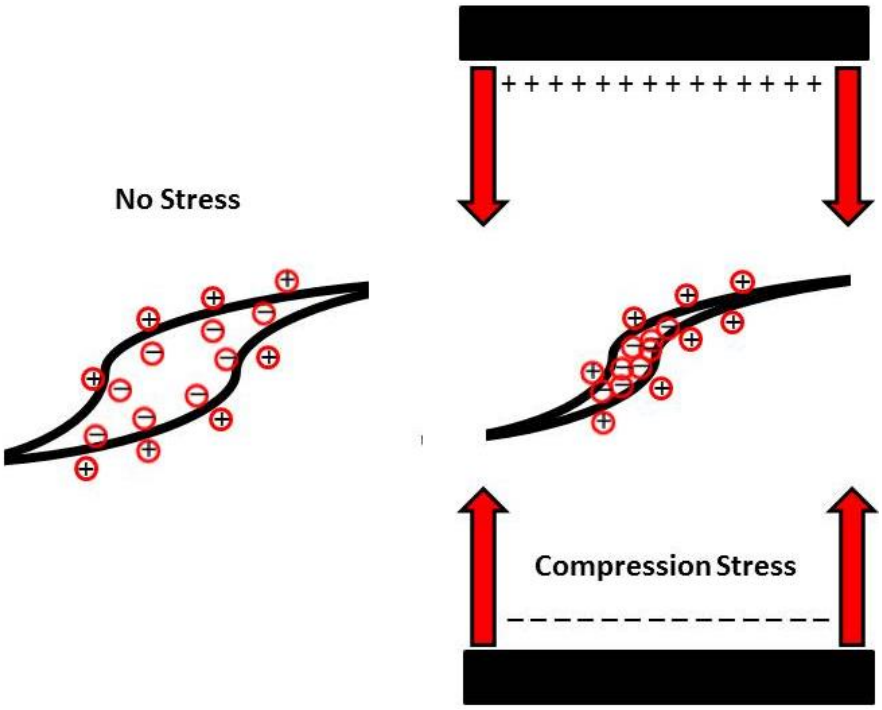

(b)

Figure 2. The piezoelectric (a), and electrokinetic (from streaming potentials) (b) effects can generate a geophysical response which can be measured in laboratory environments due to redistribution of charge, currents, electric and magnetic fields.

Laboratory stress tests on core show measurable currents ranging as a function of stress and strain from 10^{-7}-10^{-12} A depending on the composition and size of the rock under stress (Goldbaum et al., 2003; Frid et al., 2003; Triantis et al., 2008; Vallianatos & Triantis, 2008; Mori et al., 2009; Carpinteri et al., 2012). The magnetic response from these currents has been measured in experiments carried out by Freund (2002), and Carpinteri et al. (2012). The responses coincided with stress release failure events within the rock as the force on the sample was continuously increased. The magnetic measurements are larger than expected when compared to previous electric measurements; however, the mechanisms behind electric and magnetic signal generation in stressed rock are still not completely understood. Reproducing the magnetic measurement results would prove the feasibility of using magnetic methods in conjunction with electric measurements for monitoring stress/strain.

The reason so few experiments have been completed on the magnetic response due to rock under stress in comparison to the amount of studies regarding the electric response may be due to the small magnetic fields expected from the electrical currents measured in previous experiments, and the large ambient magnetic fields from power lines and Earth itself. The current study was completed to determine whether it is even feasible to conclusively measure such small signals above ambient electromagnetic noise, and to confirm whether or not the signals are actually as small as expected. The Biot-Savart law applied to the currents found in laboratory electrical current measurement experiments gives an indication of just how small the magnetic fields produced from stressed rock are expected to be. In Equation (1), μ_o, the magnetic permeability of free space in the Biot-Savart law, which is equal to $4\pi \times 10^{-7}$ Vs/Am is the theoretical reason for the small magnetic signal amplitude verses the amplitude for electric measurements.

$$\vec{B} = \frac{\mu_o}{4\pi} \int \frac{Idl \times r}{|r^3|} \qquad (1)$$

In Equation (1), $\vec{B}$, the magnetic flux density, is dependent on *r*, the distance from the current, I. Also important to note is that the magnetic field falls off as r^2, so the measurable response will decrease quickly as the distance from the current source increases.

3 Results and Analysis

The electric and magnetic data collected at Coleman Mine were analysed in early 2013, in an attempt to identify any strain related signals. The results are shown in section 3.1 Coleman Mine Datasets. No signals were identified in the analysis, however the results were applied to the development of a multi-part experiment aimed at identifying strain related signals in a mine environment. The first part of the experiment is described in detail with results in section 3.2 Above Ground Magnetic Test. A full description of the remaining two parts of the proposed three part experiment can be found in Section 3.3 Future Follow up Experiments to Above Ground Magnetic Test.

3.1 Coleman Mine Datasets

Multiple geophysical data were collected in sills 19 and 21 of the 3425 ft level of Coleman Mine (Pun, 2011). The initial intention of a DCIP survey was to see if the estimated resistivity of the rock changed throughout the survey period, reflecting changes in the stress field (e.g. due to earth tides). The voltage response of the DCIP signals were further examined to see if additional EME associated with strain or cracking events such as those described by Triantis et al. (2008) and Mori et al. (2009) were evident. Magnetic data were analysed to determine if any magnetic signals similar to those shown by Freund (2002), and Carpinteri et al. (2012) could be identified.

3.1.1 Electrical Data

The DCIP electrical data were collected along two sills, as well as down two boreholes, within each sill, using 36 electrodes. Surface electrodes were placed in 10.2 cm diameter water filled holes at a horizontal spacing of 2 m along the sill. Borehole electrodes were spaced 4 m vertically. The set-up is described in greater detail by Pun (2011). A four period, 2048 ms, castle waveform injection current was used. The first half period consisted of a positive current pulse turning on and then off, and the second half cycle was a negative current pulse turning on and off. This waveform was sampled every 0.002 s. A 25 min injection pattern was repeated starting mid-morning on each day, running until the following morning.

The voltage response of the above experiment is referred to as the electric data in this document. Electric data was analysed to determine if any strain related signals were observed during the four day measurement period. An example of a voltage response is shown in Figure 3.

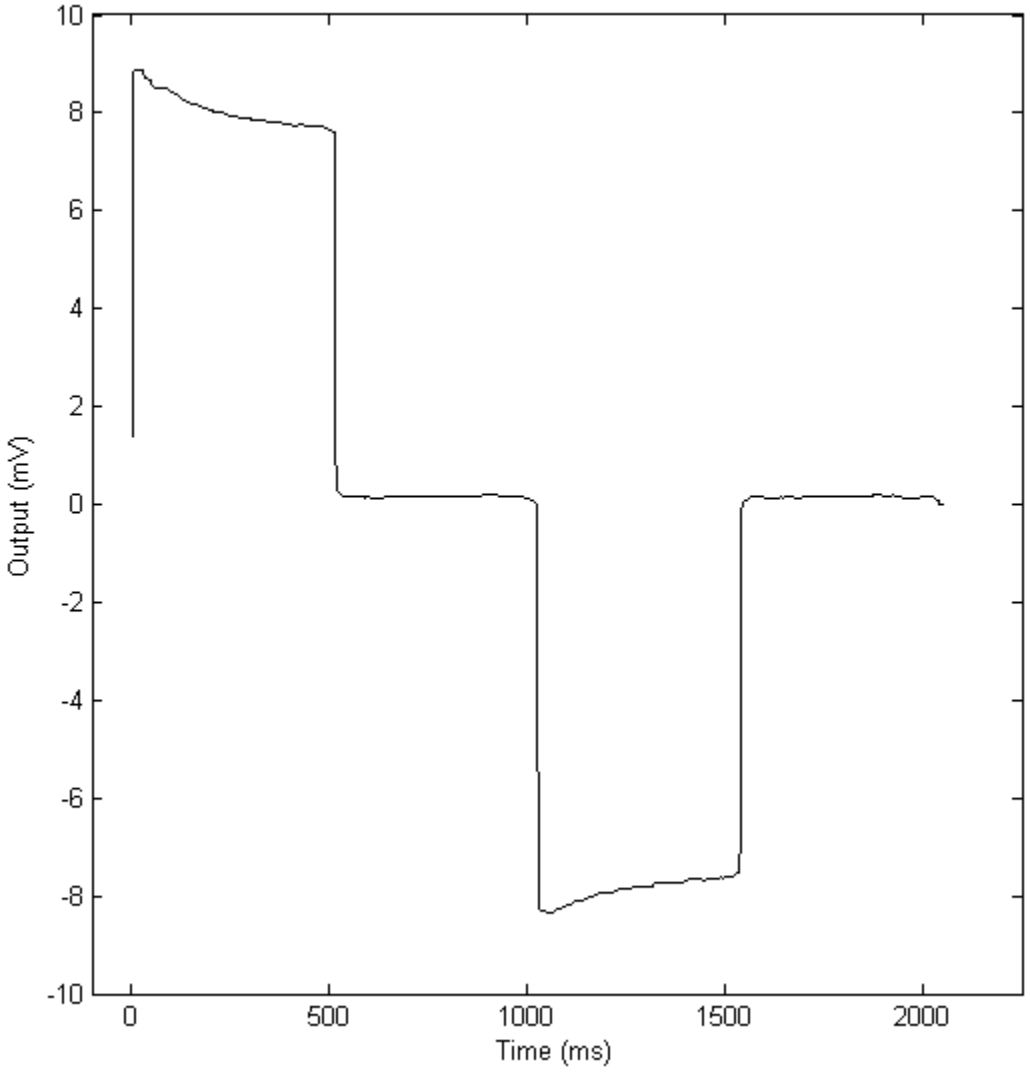

Figure 3. An example of a typical voltage response consisting of a positive, and then a negative current pulse.

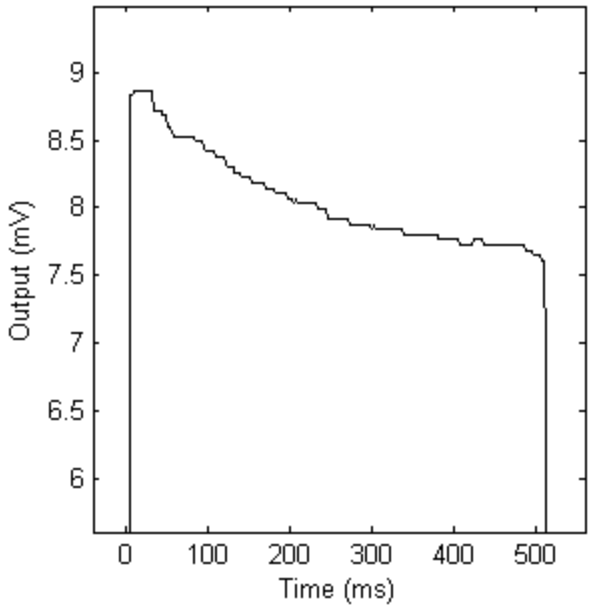

Figure 4. Zoomed in view of the first peak in Figure 3 showing the signals and noise located on-top of the voltage response from the current injection. Possible strain related signals might be located here.

The magnitude of the current injection varied from 0 mA to 185 mA. The response of the current injection is obvious in Figure 3 where any signals resulting from strain would be added to the voltage response from the current, either during the time when the current is on or off. As an example, I have zoomed in on the positive current pulse to see if any subtle small signals are evident in the close up in Figure 4. Algorithms to remove the much larger voltage response associated with the current were implemented. The most effective algorithm created an averaged waveform for each of the 168 current injections in the 25 min cycle. These average curves were then scaled to account for slight baseline shifts, due to equipment, and subtracted from the original raw curves from which the average curves were created. After subtraction only the additional signals should remain. Figure 5 shows the remnant signal with a mean of 0.003 mV

and standard deviation of 0.136 mV. Spectral analysis suggests this could be considered white noise. Some signals still showed traces of the current pulses due to imperfect subtraction, so the noise was not always white, but the mean was still near zero as expected. After spending a long time looking at the remnant signals it was deemed that anomalous signals could not confidently be attributed to strain.

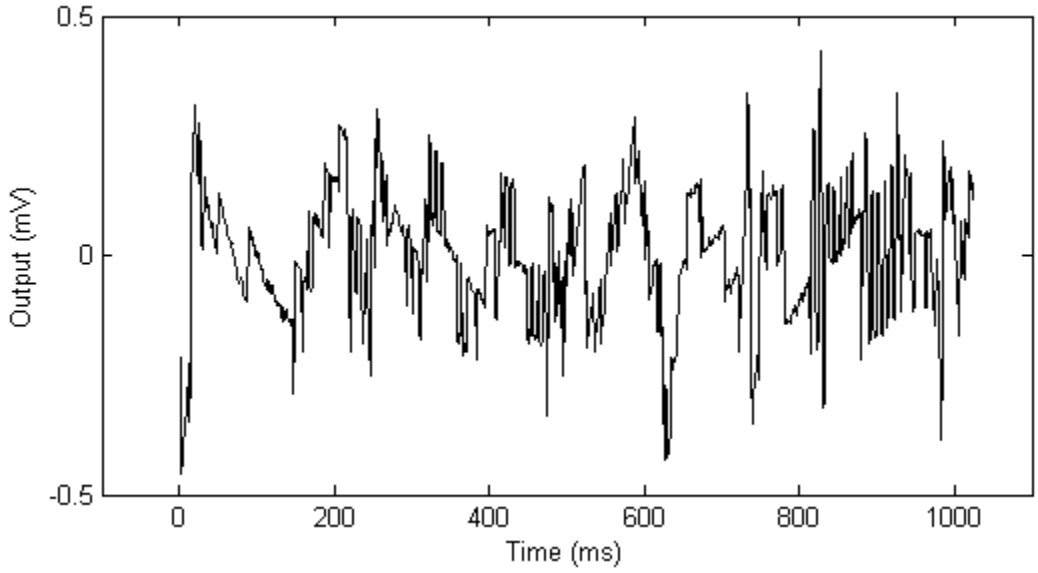

Figure 5. Voltage signal remaining after removal of voltage response associated with the current injection. Mean of example shown is 0.003 mV with standard deviation of 0.136 mV. Spectral analysis suggests this could be considered white noise.

3.1.2 Magnetic Data

Concurrent magnetic data was collected at a 0.005 s sample rate using two Ant-5 magnetic antennas located approximately 10 m behind the boreholes used for the electric measurements. As an example, a one hour segment of raw magnetic data collected from Coleman Mine is shown in Figure 6, and two shorter segments are shown in Figure 7.

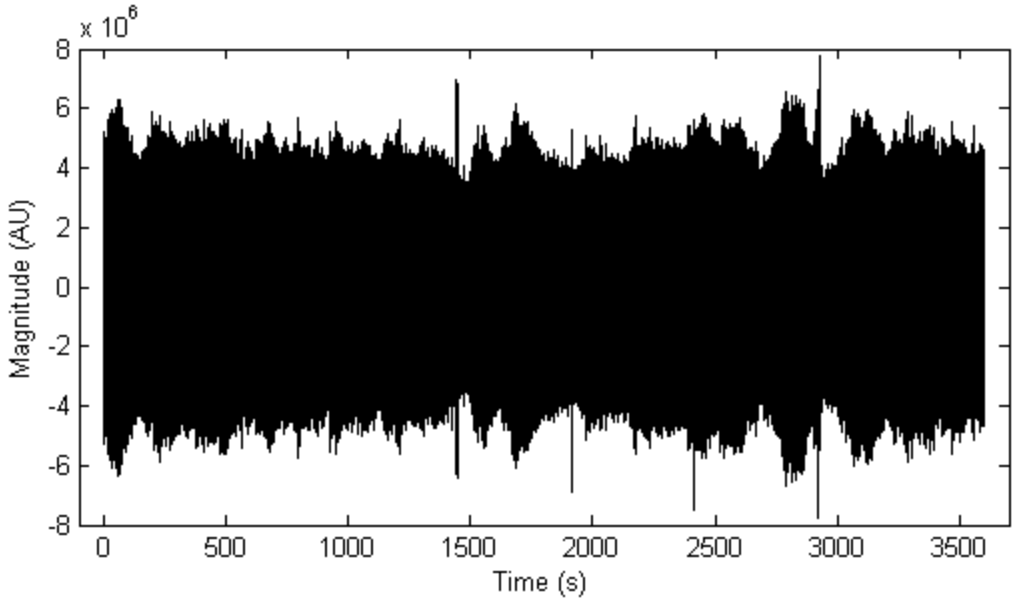

Figure 6. One hour raw segment of magnetic data collected from Coleman Mine.

On the latter, 60 Hz waveforms are evident. After filtering to remove 60 Hz powerline noise, the most obvious magnetic signal remaining in the data is a magnetic field associated with the current injection from the electric experiment carried out 10 m away. A quick comparison of a segment of magnetic data, with the current waveform is seen in Figure 8. Due to the variable success removing the effects of the current injection from the electric data, magnetic data were only examined during times of no current injection for signals related to strain events. Various anomalous signals were found in the magnetic data, examples of which can be seen in Figure 9. Due to a lack of information regarding activities in the area during data collection the signals could not be attributed to a particular source. An attempt was made to correlate seismic and blasting events evident on the micro-seismic data collected continuously at the Coleman Mine with the magnetic data set. Due to improper time stamping on one or both of the data sets, the data could not be synchronized and no comparison could be made. A comparison between seismic and magnetic datasets could have provided insight into the seismo-electric/magnetic

effect as stress related seismic events will propagate from the source at seismic velocities and these would be directly preceded by electric and magnetic signals that propagate at the speed of light. An general overview of the algorithms used for analysis of the electric and magnetic datasets can be found in Appendix A. A complete description of all research completed on the electric and magnetic datasets from Coleman Mine can be found in Appendix B.

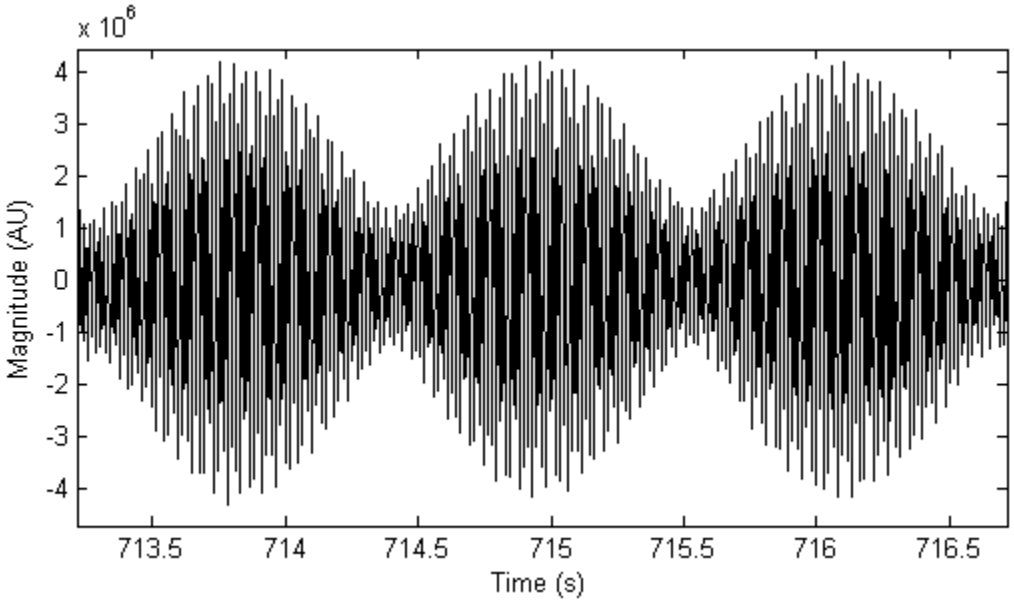

(a)

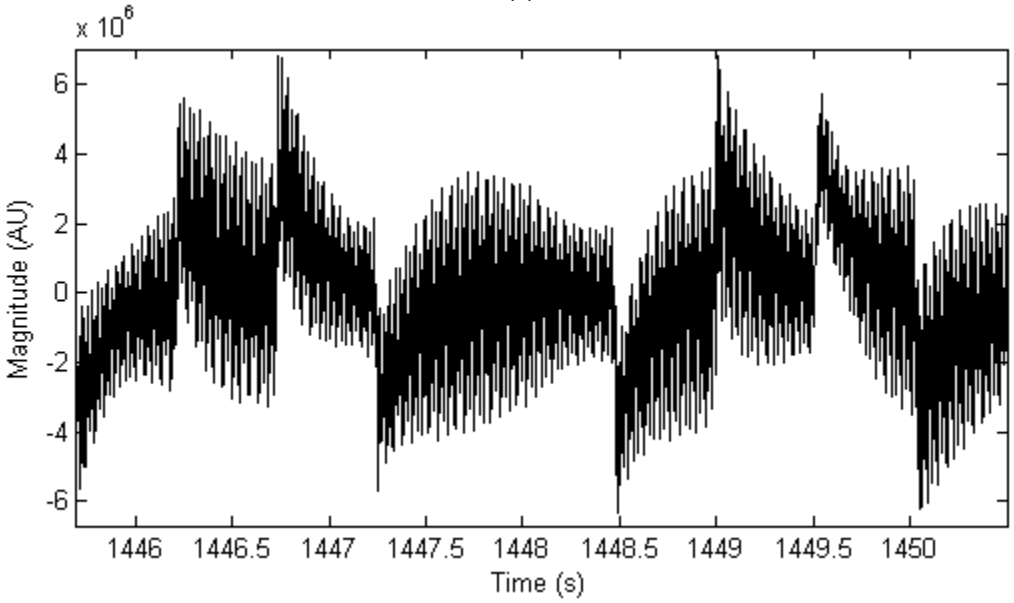

(b)

Figure 7. Two zoomed in sections (a) 715 s and (b) 1450 s into the time series. In both examples 60 Hz waveforms are present in the magnetic data before frequency filtering.

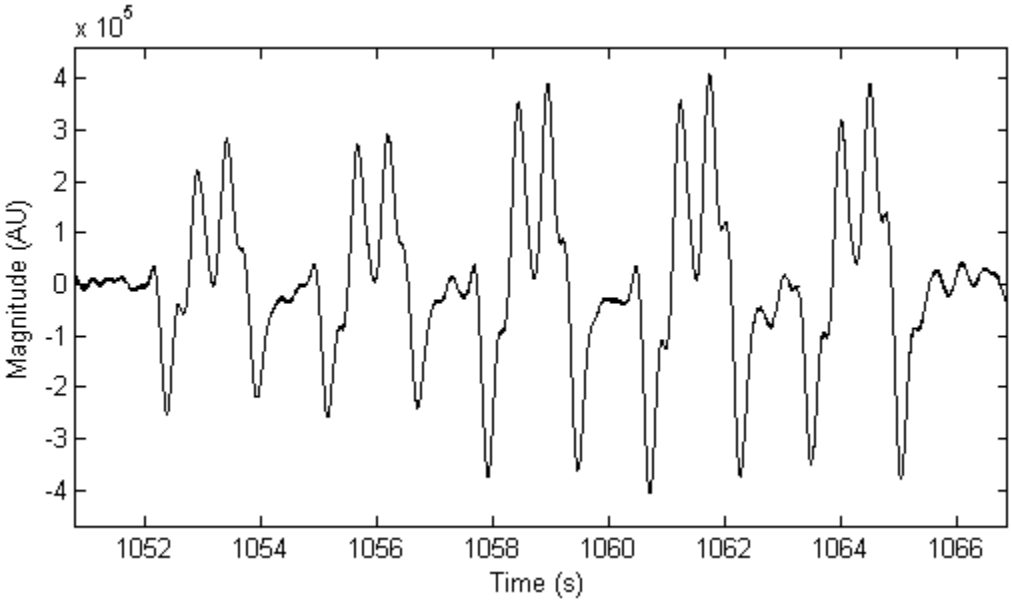

(a)

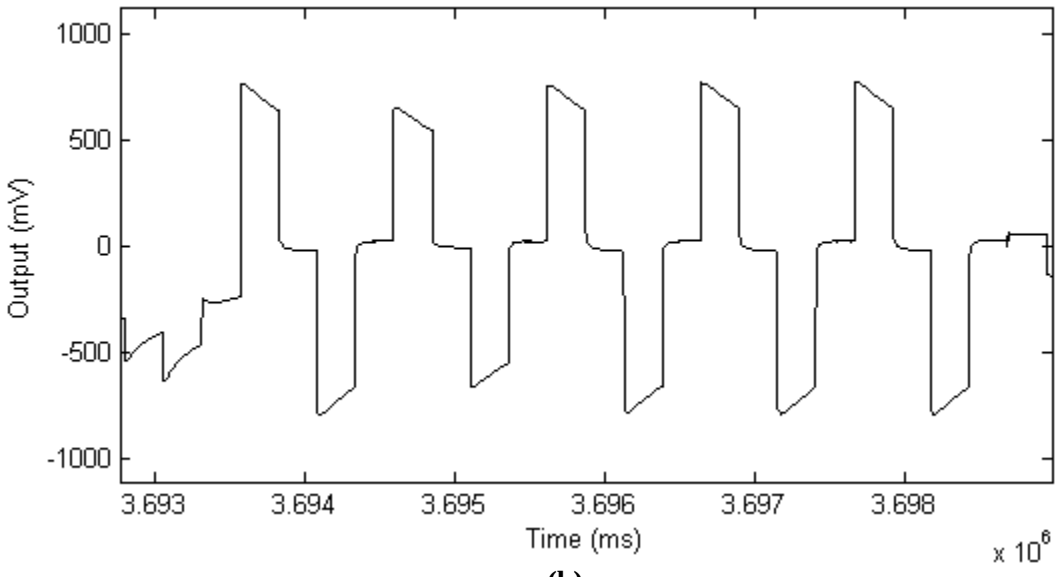

(b)

Figure 8. Magnetic data (a), and electric data (b) show the correlation between the current injections used in the DCIP experiment and the magnetic response from these injections. The variance in the magnitude of the peaks is due to the differing locations from which the data was taken. There is a difference in time because

momentary pauses between individual current injections are not included. The comparison also shows that magnetic measurements are d$\vec{B}$/dt and not $\vec{B}$.

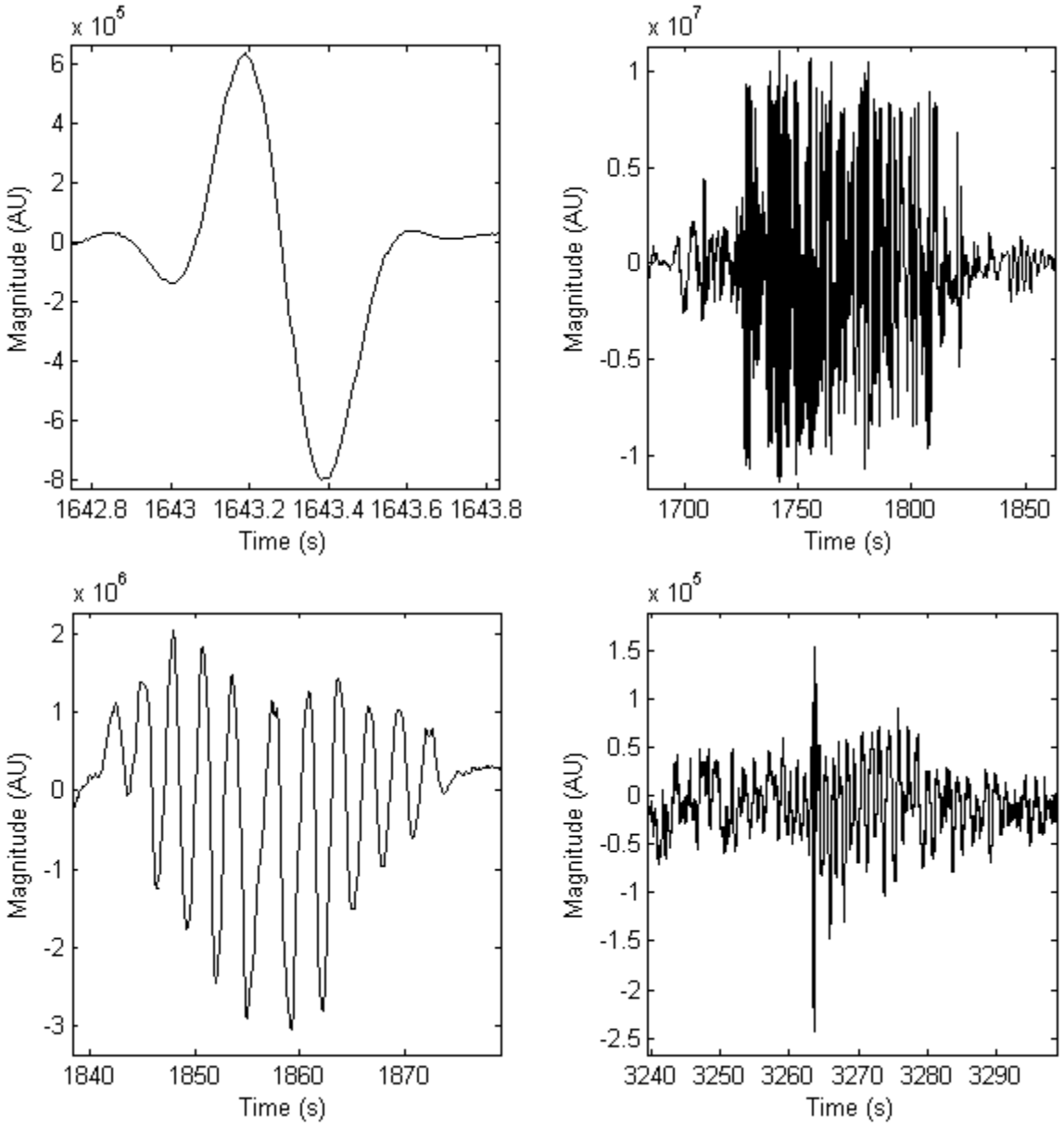

Figure 9. Four examples showing the variety of different anomalous magnetic signals found. The source of the signals could not be identified due to a lack of information regarding events occurring during the data collection period.

3.1.3 Data Acquisition Issues and Recommendations

The analysis of the electric and magnetic datasets was unable to conclusively identify any strain related signals. However, the analysis provided insight that could be used to optimize future experiments for geophysical monitoring of strain underground. Six major data acquisition issues were identified in the Coleman Mine data and are listed with possible recommendations for future data collection:

- Electric data was collected in conjunction with a DCIP experiment. Applying algorithms to remove the signal measured from the current injection may have compromised any strain related signals due to the amount of processing required. Also, the significant size of the DCIP signal meant that significantly smaller signals related to strain were not apparent in the electric data.

- Laboratory research on the electric response from rocks under stress indicates that many of these strain related events occur at frequencies above 5000 Hz. The Coleman magnetic data was collected at a 0.005 s sample rate, over a three day period, while the electric data was collected in 76158 separate 2 s intervals, at 0.002 s sampling rate. These frequencies are probably not sufficiently high for resolving strain related events. Laboratory magnetic field results are not well documented; however, magnetic events will most likely also occur at frequencies above 5000 Hz.

- As all data sets were initially collected for independent analysis no priority was placed on proper time stamping or synchronization. Although it was possible to correlate the

magnetic and electric data sets with each other through the magnetic response of the DCIP injected current, correlation with seismic events was not possible. The proprietary micro-seismic system used by the mine could not be synchronized with the electric and magnetic data collected. The ability to time correlate all data sets has significant benefits for analysis of specific events.

- Magnetic and electric (DCIP) data were collected coincidently over the three-day period resulting in interference between the two experiments. Magnetic fields from the current carrying DCIP wires were evident in the magnetic data set. Future geophysical monitoring experiments should run passively to minimize interference.

- There were no baseline measurements done on any of the instruments used for the data collection. Tests to determine the optimal bandwidth and baseline noise environment should be carried out before data acquisition. Furthermore, a base station located away from the experimental site to collect background readings should be deployed to aid in future analysis. This would be used to identify EME events not associated with stress events such as distant lightning strikes, known as sferics. Without this information prior to data collection it is difficult to identify and attribute all the various signals in the data.

- Operational noise sources within the mine were not documented. This includes but is not limited to sump pumps, movements of the cage, drilling, blasting, ventilation, and people or vehicles passing by the test site. For proper data analysis as many sources of electromagnetic, acoustic, and seismic noise must be noted.

3.2 Above Ground Magnetic Test

A multi-part experiment aimed at identifying strain-related signals simulating those that might occur in a mine environment was developed from the lessons learned during the analysis of the data from Coleman Mine. The first part of the experiment was completed April 26th, 2014 in parking lot 15 located on the Laurentian University campus, Sudbury, Ontario. In the experiment a total of thirty-two core samples, consisting of eleven different lithologies, were stressed until failure using a load frame. Magnetic coils located around the load frame were used to measure any potential magnetic fields induced when the core was stressed.

The thirty-two rock samples were stressed to failure by applying periodic pressure increases. Base station magnetic measurements, taken 19.5 m from the load frame were used to confirm that any signals found in the data originated from the load frame.

3.2.2 Equipment and Location

The magnetic field sensors surrounding the steel load frame were Ant-3 magnetic antennas (designed for geophysical exploration) with sensitivity to frequencies up to 32 kHz. The magnetic coils at the base station, 19.5 m from the load frame, were also Ant-3 antennas. Both locations were intended to acquire data at 32 kHz; but this was adjusted due to technical difficulties with the base station data acquisition unit only being able to acquire data to 9 kHz on the day of the experiment. The instruments ran passively and independently with built in atomic clocks (GPS synchronized), and battery packs so no external power resources were required. The data acquisition unit for the magnetic coils was a three-channel system allowing measurements to be collected in all three x, y, and z coil orientations simultaneously. For completeness, atmospheric temperature and pressure data were collected throughout the entire measurement period.

A load frame was used to apply stress to the rock samples. A hydraulic hand pump was used in lieu of the nominal air compressor to reduce noise. The load frame was capable of applying stress levels above that required to bring the rock samples to failure. The pressure applied across the core was recorded manually from the built in gauge.

A video camera was set up zoomed in on the core and platens to monitor platen movement throughout eight tests on various rock samples. The camera was implemented as a quality control measure for monitoring sudden platen movement from pressure variation as a result of rock failure during experimentation. Due to video quality through the protective Plexiglas®, and movement of the camera from a slight breeze, platen movement could not be accurately monitored. The video has however been used to help with identifying the exact moment of sample failure; this was less clear in the images than was initially expected, but cracking sounds were clear in the audio track.

The parking lot used was approximately 100 m away from the nearest building and is lined by minimal lighting and power lines. The tests were undertaken on a Saturday morning, when there were no vehicles present. Figure 10 shows the experimental set-up used to carry out all tests on the rock samples.

Figure 10. Experimental setup located at Laurentian University, Sudbury, Ontario. Pictured is the load frame surrounded by magnetic coils. The two horizontal orthogonal coils on the left were buried in snow, and the vertical, to the right, sunk into a bucket of sand to increase stability.

3.2.3 Rock Types and Sample Preparation

A representative suite of ten rocks from the Sudbury area were selected for the experiment in addition to a marble sample to compare with the results of Triantis et al. (2008). Attempts were made to limit ore mineralisation within the rock samples.

The rock types tested were 1) Hornblende (Hb)-Biotite (Bi)-Granite, 2) Hb-Bi-Quartz (Qtz)-Monzodiorite, 3) Hb-Bi-Pyroxene (Px)- Pyrrhotite (Po)-Norite, 4) Bi-Hb-Tonalite, 5) Marble, 6) Hb-Px-Mafic Dyke, 7) Bi-Hb-Qtz-Monzodiorite, 8) Hb-Bi-Po-Norite, 9) Bi-Plagioclase-Gneiss, 10) Epidote-Qtz-Alkali Feldspar-Syenite, 11) Bi-Pyrite-Syenite. The samples were core samples with diameters from 2.5 to 5.0 cm cut to lengths of approximately 25.4 cm. Each of these rock

types were represented by multiple samples; the sample numbers are given in Table 1. Exact dimensions for each sample, their mineral constituents, depth retrieved from, and grain size can be found in Table 2 in Appendix C. Images of the various rock types are shown in Figure 11.

To avoid shear failure, samples with minimal to no structure were selected for the experiment. In an attempt to ensure only an axial force across the samples, all samples were first cut to length using a diamond saw, before the ends were ground flush with a lathe. To isolate charge movement to the rock sample being stressed, the samples were all insulated from the steel load frame on each end using a thin layer of electrical tape.

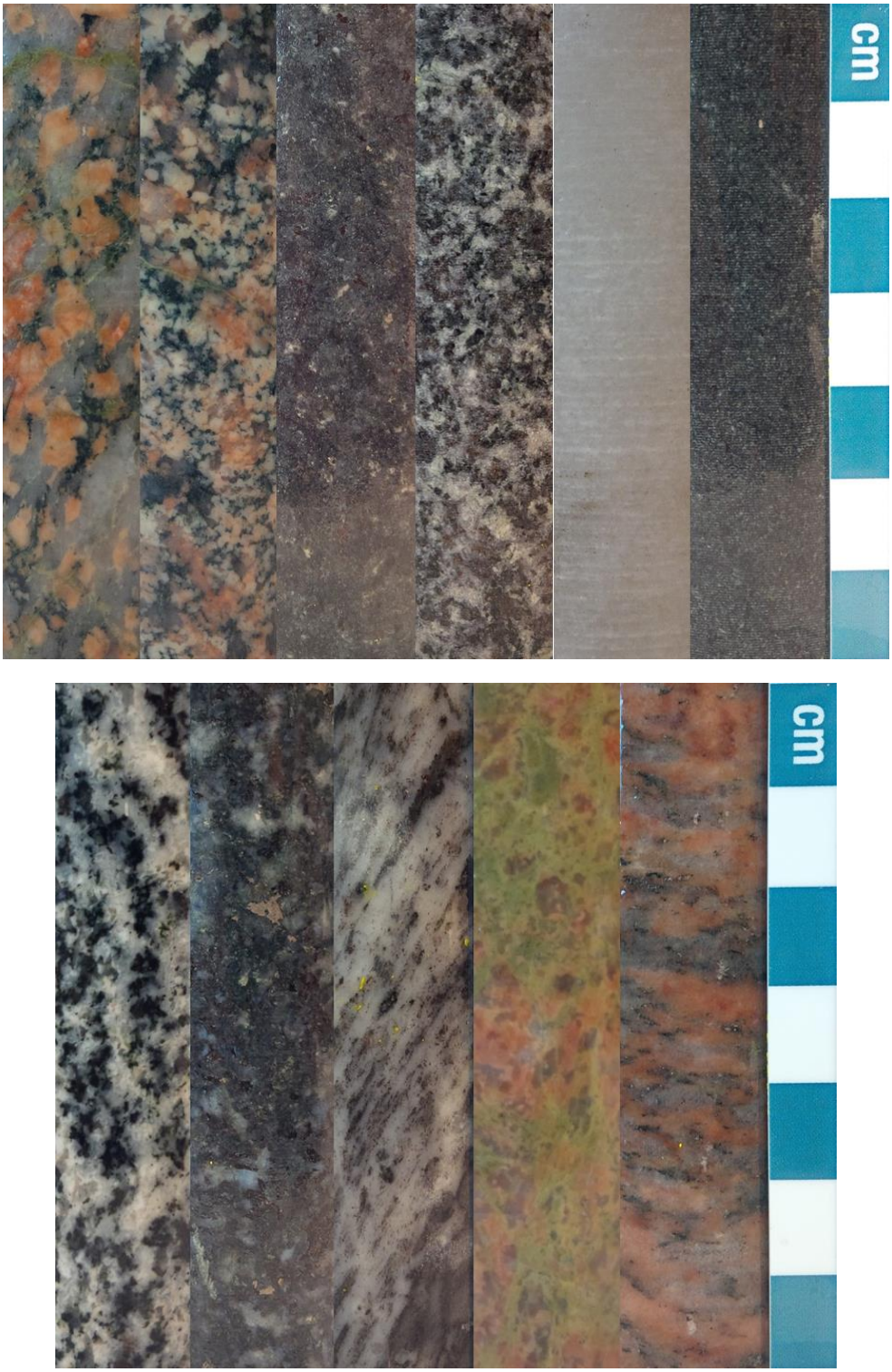

Figure 11. Photographs of all rock types used for the experiment. From top left to bottom right: Hb-Bi-Granite, Hb-Bi-Qtz-Monzodiorite, Hb-Bi-Px-Po-Norite, Bi-Hb-Tonalite,

Marble, Hb-Px-Mafic Dyke, Bi-Hb-Qtz-Monzodiorite, Hb-Bi-Po-Norite, Bi-Plagioclase-Gneiss, Epidote-Qtz-Alkali Feldspar-Syenite, Bi-Pyrite-Syenite.

3.2.4 Orientation of the Magnetic Coils

To measure the entire magnetic response from core under stress, three magnetic coils were oriented perpendicularly in the x, y, and z coordinate system. Deploying three coils ensured there was a minimal chance of null-coupling to magnetic fields. To reduce interference, the coils were arranged around the load frame at equal distances from the core as shown in Figure 10. To mitigate noise generated by wind moving the coils and changing the flux of the earth's magnetic field, the two horizontal coils were buried under snow, and the vertical coil was sunk into a sand filled container. This meant it was not possible to arrange the coils in the optimal arrangement, on the same plane of measurement with the core sample being stressed.

3.2.5 Base-Station Measurements

Base-station measurements were taken 19.5 m from the centre of the load frame in the same x, y, and z coordinate system as the coils surrounding the load frame. Each base-station coil acquired data at frequencies up to 9000 Hz. As the base station was set-up in a snow bank, all the base station coils were buried in snow. The base station was set-up far enough from the main experiment that no signals related to strain should have been measured, yet, close enough that the ambient magnetic fields in the area can be considered comparable to those at the load frame. This set-up was used with the hope that data collected at the base station could be subtracted from the data collected surrounding the load frame, removing the ambient background noise. This technique is most effective when any magnetic fields in the area are slowly varying as a function of distance. Unfortunately re-sampling load frame data from 32 kHz to 9 kHz created slight variances in the time stamping of points which complicated accurately subtracting the

datasets. Thus, the base station was used mainly to visually exclude any signals that appeared in both the load frame and base station datasets. Further analysis and processing would be required for accurate subtraction of the two datasets.

3.2.6 Identifying and Mitigating Sources of Magnetic Noise

As the magnetic fields expected from rock under stress are very small, special care was taken to mitigate all controllable sources of magnetic noise. All metallic and signal-emitting personal belongings were removed from all people at the experimental site. As an added caution, persons were not permitted to move around throughout any of the measurements as it was found that walking around the experimental area created long wavelength noise in the datasets.

However, some of the sources of magnetic noise were more difficult to control. Tests without rock samples in the load frame were completed to generate instrumental signals for identification and possible removal from the data. Potentially the largest of these was the magnetic response from the movement of the platens within the load frame. As core is stressed in the load frame, the platens supporting the core move slightly and could create magnetic disturbances. When failure events commence, the movement of the platens can sometimes become erratic, due to sudden pressure drops. In an attempt to simulate the magnetic effects of the platen movement, the platens were cycled nominally up and down to create a situation in which similar magnetic responses to those produced during loading of the rock samples. The commencement of sample failure was also mimicked with quick jerk-like platen movement. Some of these signals were successfully identified and classified as non-strain related in the data, however, further research with wood or plastic samples should be carried out to confirm the results.

Another unavoidable source of magnetic noise was produced from the up and down handle motion on the hydraulic pump. Similarly to above, the load frame was cycled up without any

rock sample to generate these signals so they could be identified in the cases where samples were present. In an attempt to separate the signal produced from the hydraulic pump handle from that of the platen movement, the hydraulic pump was moved incrementally closer to the load frame during the sample-less test. As the response from the platens should remain constant, moving the pump incrementally closer could allow the response from the handle to be isolated and quantified. The effects of the pump handle were found to be low-frequency events which were easily removed from the data via the application of a high-pass filter, or temporal derivative. Platen movement was unidentifiable in the data.

3.2.7 Application of Stress with Load Frame

Although the load frame was designed to apply constant increasing pressure using an air compressor, due to the vibrational and electromagnetic noise sensitivity of the magnetic coils, a hydraulic hand pump was used instead. The drawbacks of such a set-up include repeatability as the rate and magnitude of the force applied across the core throughout each test was dependent on the person operating the pump. For this reason, the person pumping was kept the same for every sample, and efforts were made to keep the force applied consistent. All samples were stressed with periodic pressure increases of 620 kPa/s, on average, with 10 s pauses between every 3.5 MPa increase in pressure.

3.2.8 Result of Above Ground Magnetic Test

Thirty-two rock samples, a minimum of two from each of the samples listed in Section 3.2.3 were successfully tested, by applying stress until failure was reached. Post failure images of marble, mafic dyke, and biotite-pyrite-syenite are shown in Figure 12 (a) – (d). Uniaxial failure was observed in twenty-nine of the samples, while shear failure was observed in three.

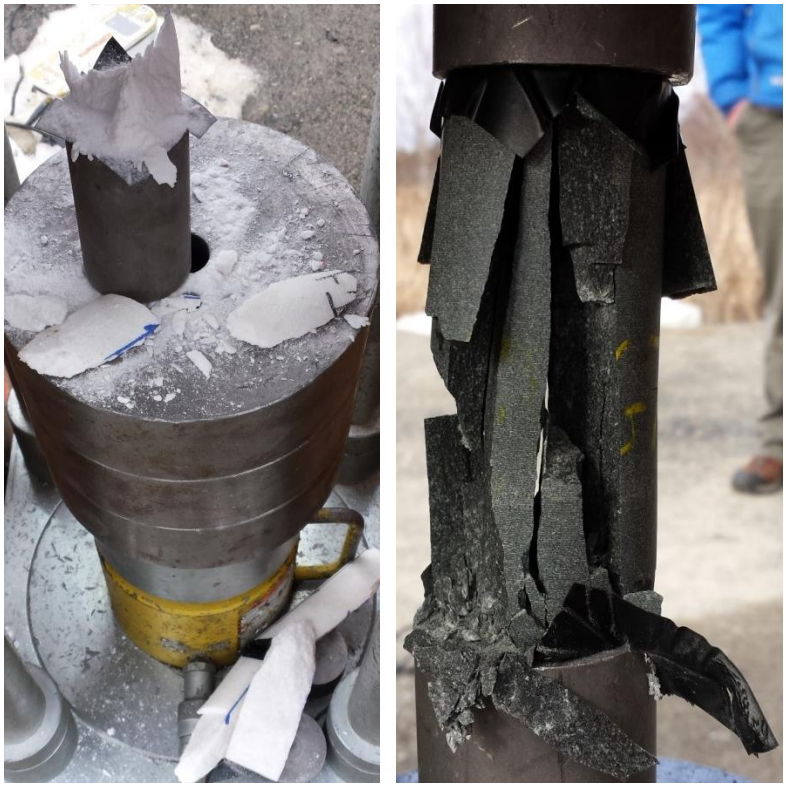

(a) (b)

(b) (d)

Figure 12. Samples of marble (a), mafic dyke (b) and biotite-pyrite-syenite (c) post failure showing uniaxial fracturing; and marble (d) showing shear fracturing.

An example frequency spectrum of the data before the removal of 60Hz powerline noise and its even and odd harmonics is shown in Figure 13 (a), and after removal is shown in Figure 13 (b). The increase in thickness of the black zone seen at the higher frequencies in (b) is due to the large number of even and odd harmonics in the higher frequencies. When all these harmonics are removed, they are replaced with a large number of strong downward notches at the location of the harmonics. Some signal from the lower powerline harmonics is evident in the data due to the signal being slightly off frequency; however, the benefits gained from applying wider notch filters surrounding these lower frequencies are not significant.

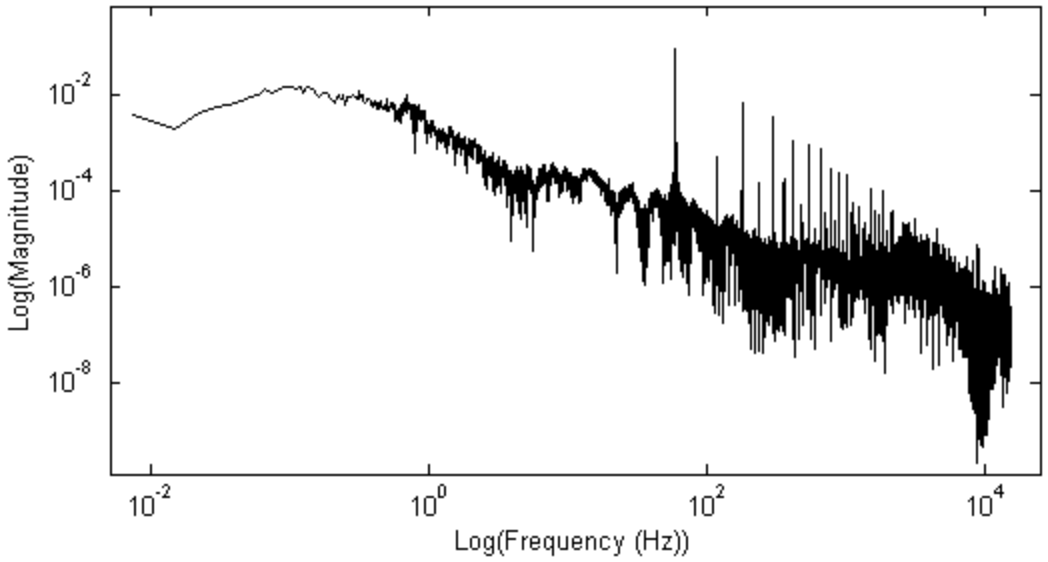

(a)

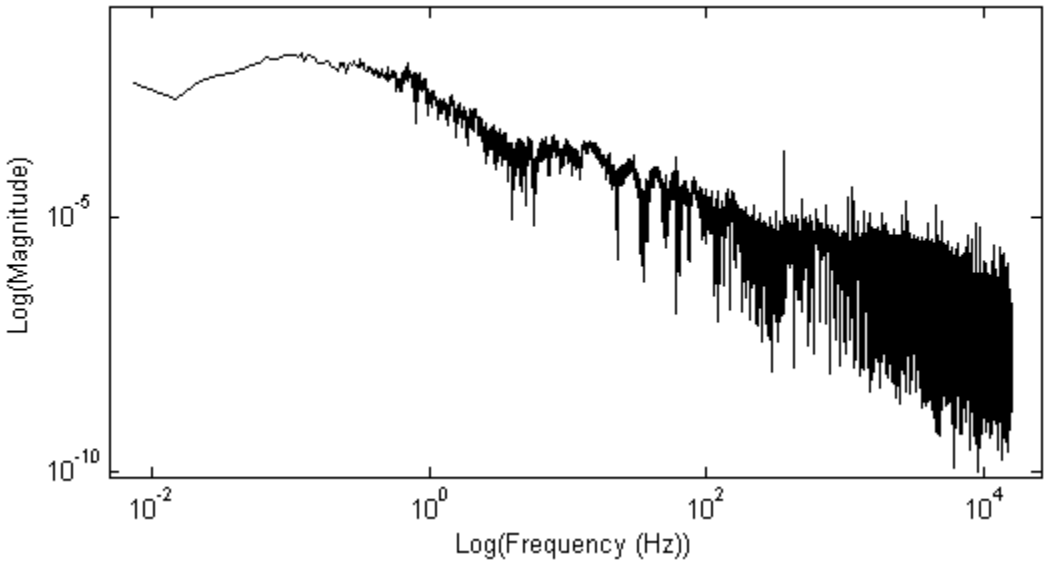

(b)

Figure 13. Log-log frequency spectrum of magnetic data for the rock sample Hb-Bi-Granite, Sample A4, (panel a) and the same sample after the removal of the 60 Hz peak and respective even and odd harmonics due to powerline signal (panel b).

Raw magnetic field time series data respectively, before, and after the removal of 60 Hz and respective odd and even harmonics for sample A4 (Sample description available in Table 2), are shown in Figure 14 (a) and (b). Unless otherwise stated all data shown is from the x (northward) coil orientation. Periodic oscillations every 10 s starting at approximately 3, 19, 35, 50, 65, and 83 s in the data on Figure 14 (b) are due to the motion of the pump handle, and/or oil in the pumping lines when increasing the pressure across the sample in 3.4 MPa increments. These signals are similar to the signals seen in the control experiments with no samples. Visible failure of the sample is indicated by the red line at 91.25 s which was determined from video taken during the loading of the sample. This red line coincides with a broad positive peak in the magnetic field. A similar visual analysis to determine the moment of sample failure was carried out for samples F3, F4, A3, E3, E4, G6, and G7, as these were the only samples for which video was recorded. The large negative peak, at 91.0 s, appears with similar sign and magnitude prior to the failure of each respective sample. The moment of complete sample failure, manually extrapolated from video where available, consistently falls at the apex of the second broader positive peak. From this information it was assumed that failure occurred at the second peak for all samples for which no video recording was available.

The large sharp negative (91.0 s) and the more broad positive (91.25 s) peaks were initially thought to be due to the magnetic fields induced at failure due to the falling of platens. The G7 sample of mafic dyke, shown in Figure 12 (b), did not fall, so the platens remained supported. Figure 15 shows a very similar magnetic profile at failure, supporting the idea that these peaks are potentially rock failure or equipment related rather than from the falling of platens. It is important to note that sample G7 did not behave as G1, G2, and G6, the three other samples taken from the same length of core, failing after far less audible cracking, at a lower pressure,

resulting in a lower uniaxial compressive strength (see Table 1). Although sample G7 is the only sample for which platens remained in place. I conclude that falling platens likely do not cause the negative and positive magnetic peaks.

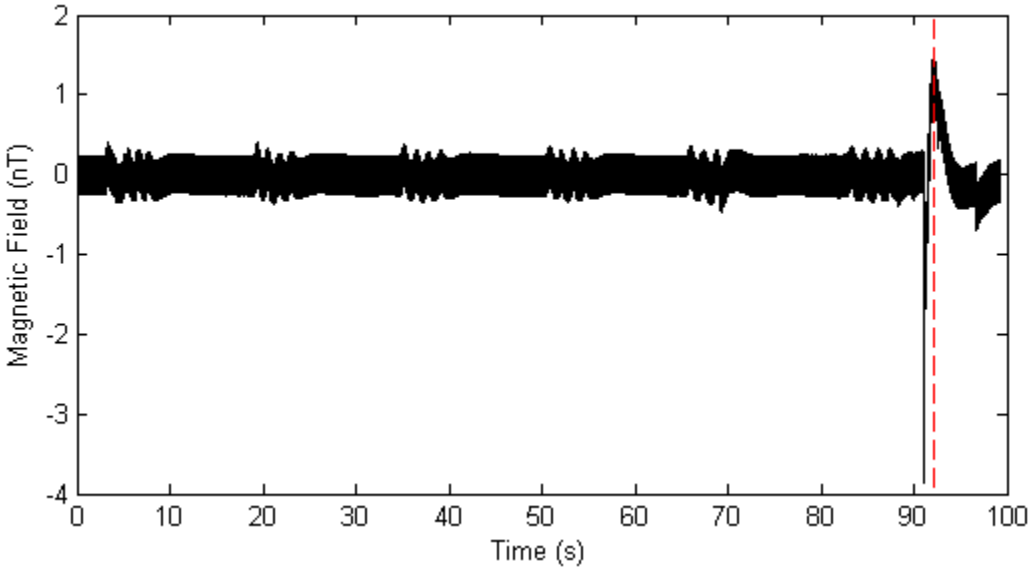

(a)

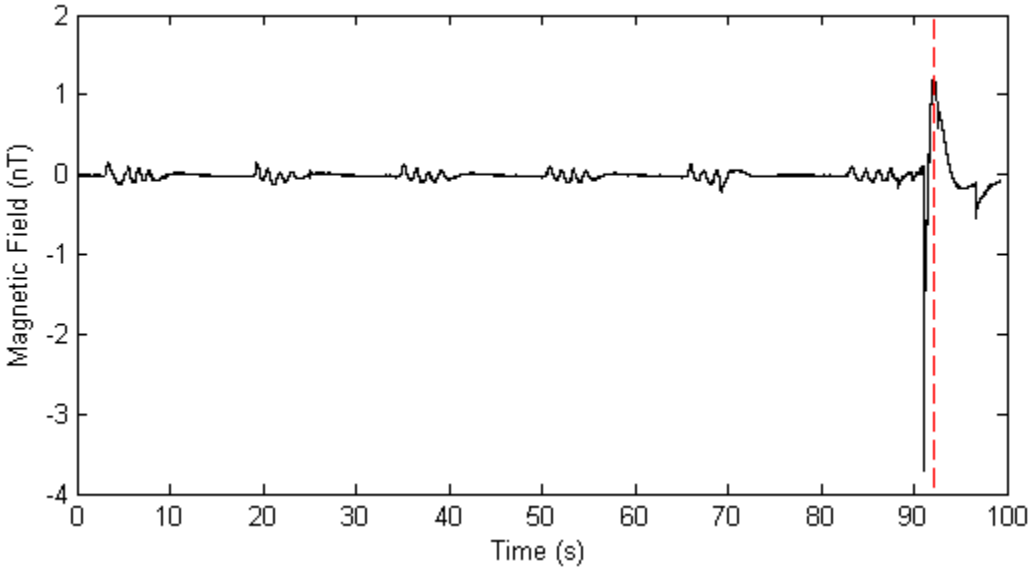

(b)

Figure 14. Magnetic field data for sample A4 (a) Raw and unfiltered, and (b) after the removal of 60 Hz and respective odd and even harmonics. Oscillations appearing every 10 s in both datasets are due to the motion of the pump handle when increasing the pressure

across the sample. Failure of the sample (from video) is indicated by the red line at 91.25 s.

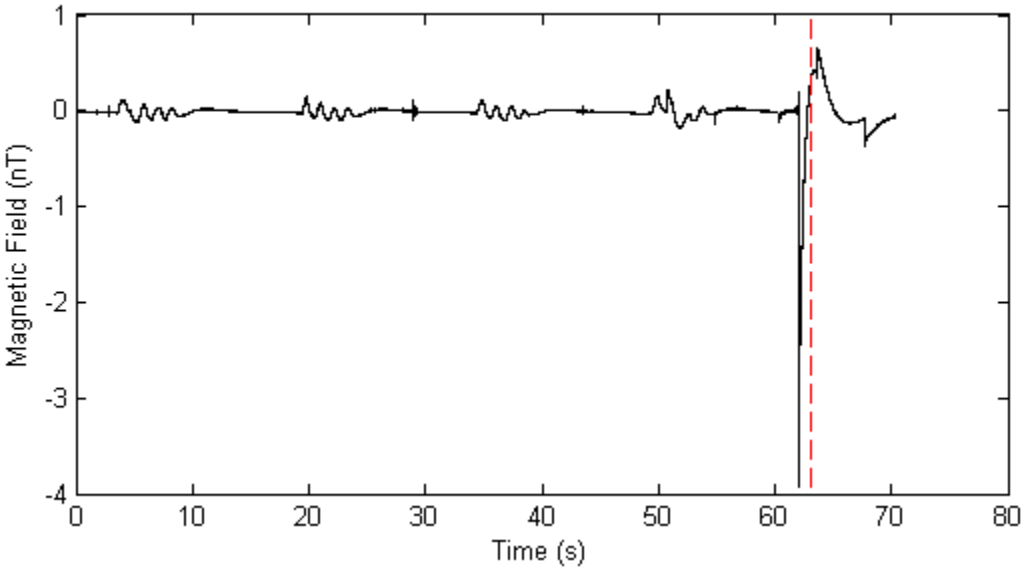

Figure 15. Magnetic field data for sample G7 for which the platens and the sample did not fall after failure. Compared with Figure 14 (b) a slight variation in the profile at failure (63.12 s) is visible, however the general shape and timing of the signal is similar to those observed when platens and sample did fall. This suggests that the signals observed at failure are potentially due to rock failure or equipment, and not the falling of platens.

Using the video and associated audio recordings for samples F3, F4, A3, A4, E3, E4, G6, and G7 the times of audible cracking that occurred throughout the loading process was recorded. A unique magnetic signal was found to occur during periods of audible cracking, and also during the second before visible failure. Two of these unique signals are evident in the frequency vs time plot (Figure 16), highlighted with a red ellipse. A close up of the two anomalies are shown in Figure 17. A second set of unique magnetic signals which did not seem to correlate with any

strain or pumping related activities are also identified in yellow on Figure 16. A time domain example of this second type of signal is shown in Figure 18. The characteristics of these signals are similar to sferics.

The time-domain plot of the first signal identified in red in Figure 17 is shown in Figure 19. The strength of the example shown is abnormal. Generally signals are difficult to identify in the time series magnetic data as they are sometimes almost completely lost in noise. Signals do not usually contain obvious oscillations with a period of 0.006 s as the example shown. With the application of a temporal derivative to the time-series magnetic data these types of signals of interest are far easier to identify. An example of such a signal is shown in Figure 20. The unique frequency spectra of the signals of interest allows them to be easily distinguished from other signals which can sometimes look similar in the data, such as the signal shown in Figure 18. A general description of all the algorithms used to analyse the magnetic data can be found in Appendix D. The picking of signals, and some of the other more common signals found in the data are discussed in Appendix E.

All of the signals of interest found for the sample A4, Figure 14 (b) are indicated in Figure 21 by black arrows. Thicker black arrows are due to regions with multiple signals stacking on top of each other. As mentioned, these signals only appeared during audible cracking as is also shown with vertical lines in Figure 21. Magenta lines indicate the onset of audible cracking, green lines their cessation. The final green line also indicates the moment of visible sample failure. Samples which undergo failure with no audible precursor show no signals of this form until the second before fracture. Similar results for samples F3, A3, E3, E4, G6, and G7, the remaining samples for which there were audio recordings, can be found in Appendix F.

Note, although an audio recording was available for sample F4, no figure is shown in Appendix F, as no signals of interest were found in the dataset. A recurring trend for the remainder of the document is the unpredictability of the marble samples, F1, F2, F3, and F4. These samples were the only which were not igneous, or metamorphosed from an igneous sample. The audio recording of sample F3 does contain some faint cracking sounds right at the moment of failure, although that of sample F4 does not. It should be noted that the wind at the time of data collection for samples F3, and F4 was higher than for other samples making it more difficult to hear any audible cracking. A further discussion on the marble samples can be found in Appendix G.

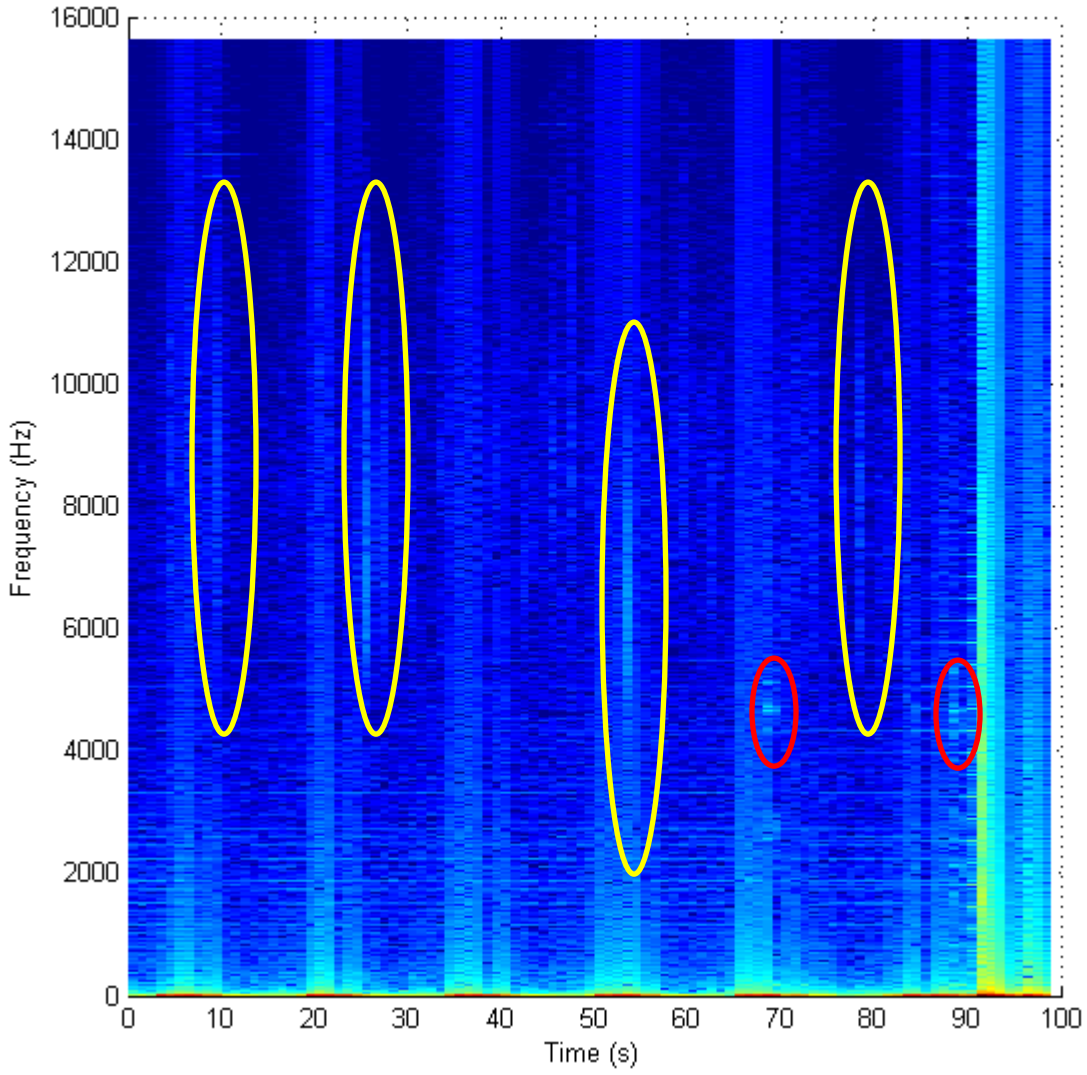

Figure 16. Frequency as a function of time graph shows two distinct types of frequency anomalies. The first, identified in red, found at approximately 4700 Hz and just less than 70 s and just after 90 s is a group of signals found only during audible cracking. The second, identified in yellow, does not seem to correlate with any sort of strain event.

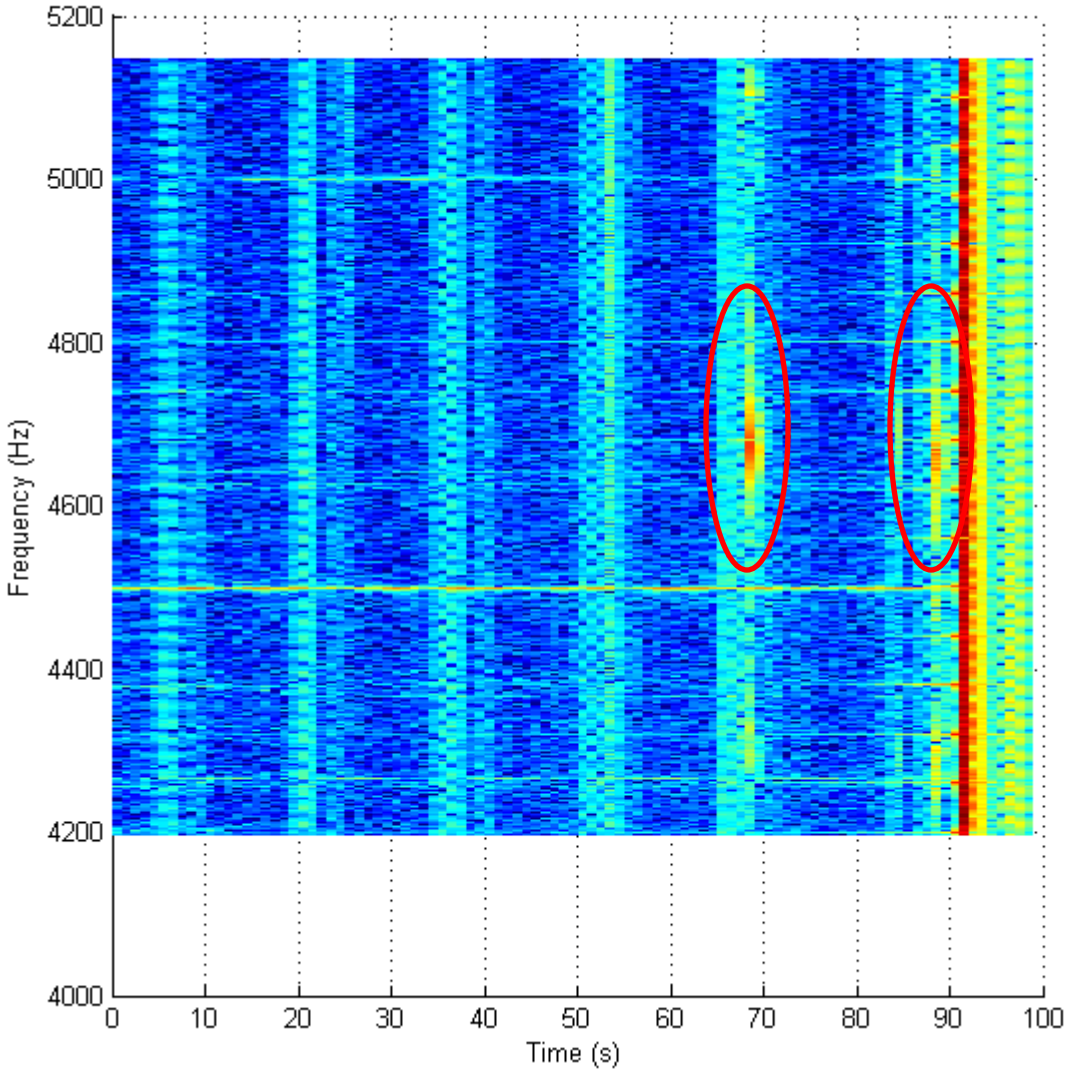

Figure 17. Close up of Figure 16, frequency as a function of time graph, better identifying in red the signals found at approximately 4700 Hz and just less than 70 s and just after 90 s which correlate with audible cracking.

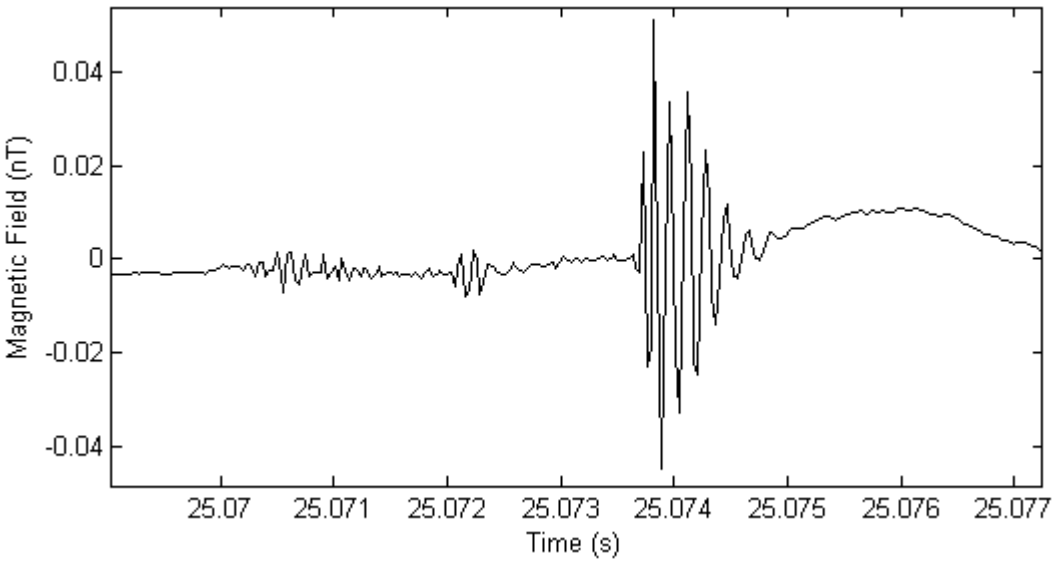

Figure 18. Time domain example of signal identified in yellow in Figure 16. These signals do not seem to correlate with any obvious strain or instrumental activities. The signals always appear very similar in appearance.

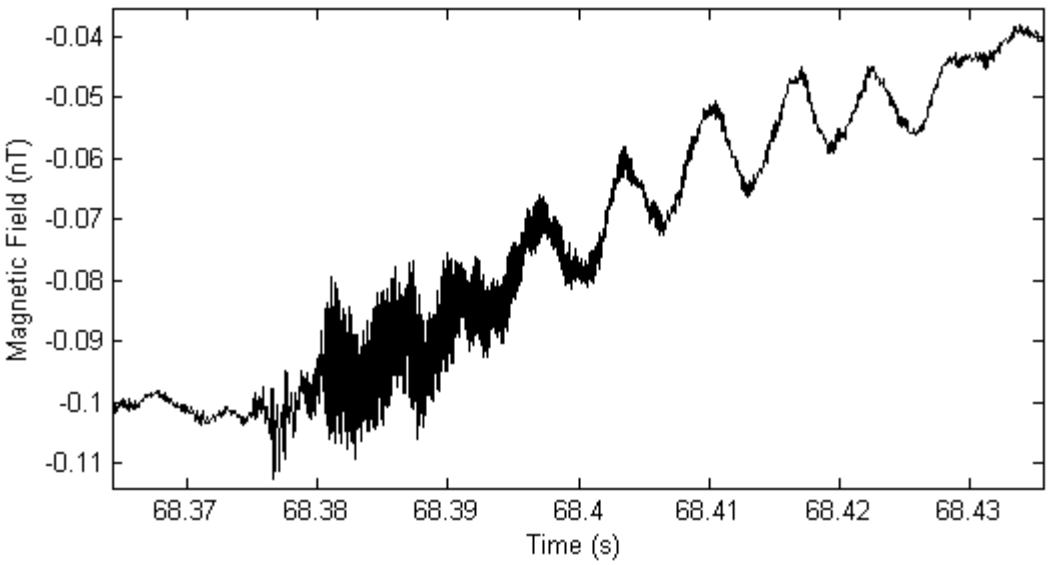

Figure 19. Time domain example of signal identified in red in Figure 16. These signals only appear during audible cracking. The cause of the oscillations with a period of 0.006 s is unknown and does not show up in all magnetic signals.

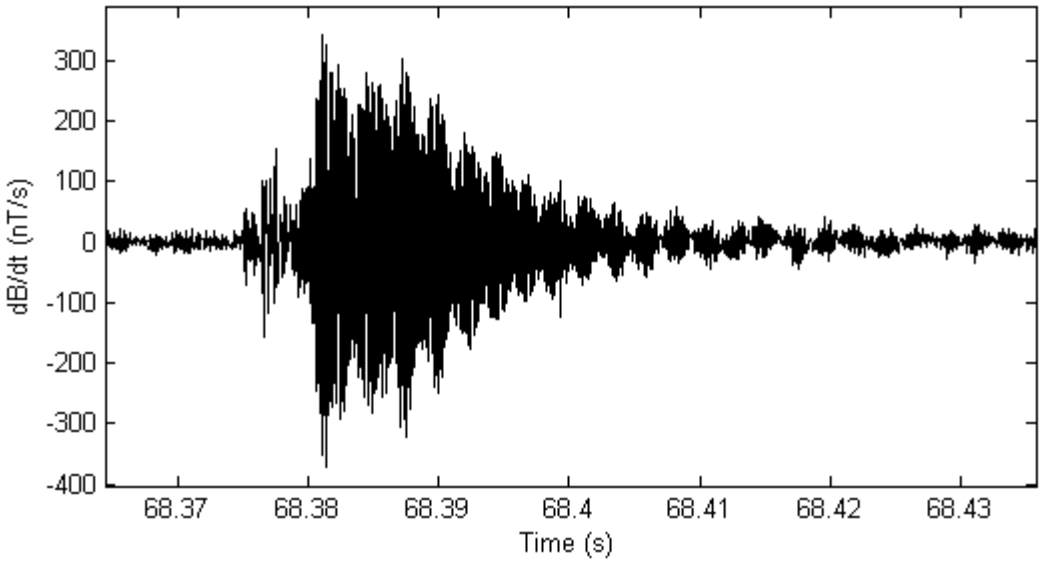

Figure 20. Signal of interest shown in Figure 19 after the application of a temporal gradient, which makes identification of the signals easier.

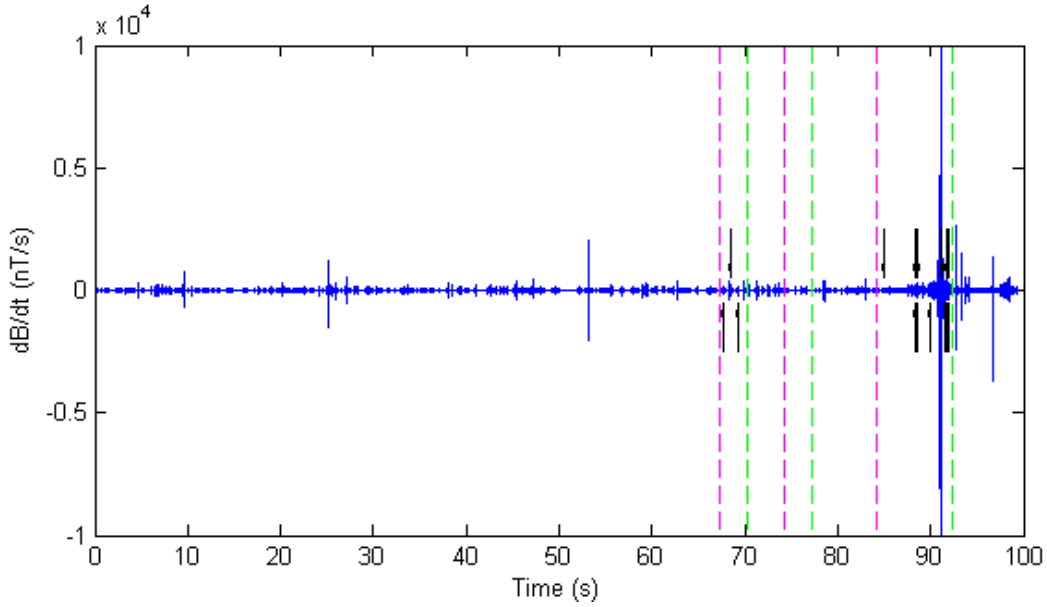

Figure 21. Temporal gradient of Figure 14 (b) shown in blue. Magenta lines indicate the onset of audible cracking; green lines indicate their cessation. The final green line also indicates sample failure. Black arrows indicate signals as shown in Figure 20

appearing in the data. These signals are only apparent during or near audible fracturing. Thicker black arrows are due to regions with multiple signals occurring close to each other.

All data, and signals of interest, shown thus far, were collected in the x-coil orientation. The signals do not always show up in all coil orientations, however, when they do, they always appear slightly different. Figure 22 (a) shows one example of different signals. The data for the x-coil orientation is shown in black, y-(eastward)-coil orientation in red, and z-(vertical)-coil orientation in blue. Zooming in on the yellow area, Figure 22 (c), it is evident that there seems to be no signals of interest in the y, and z orientations. This is contrary to that seen zooming in on the green area, Figure 22 (b), where although not as pronounced as in the x orientation, signals of interest are visible in the y, and z orientations.

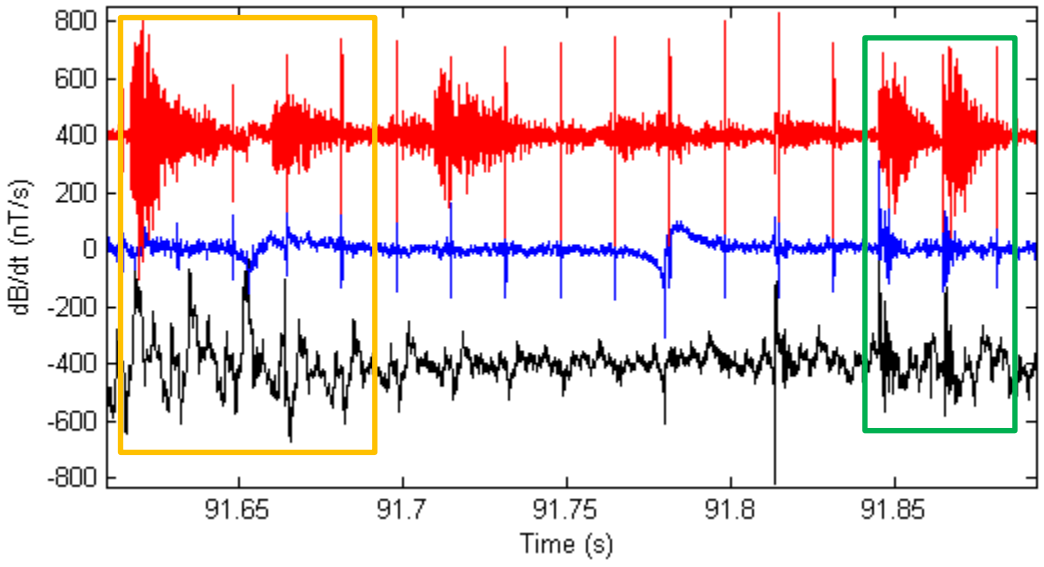

(a)

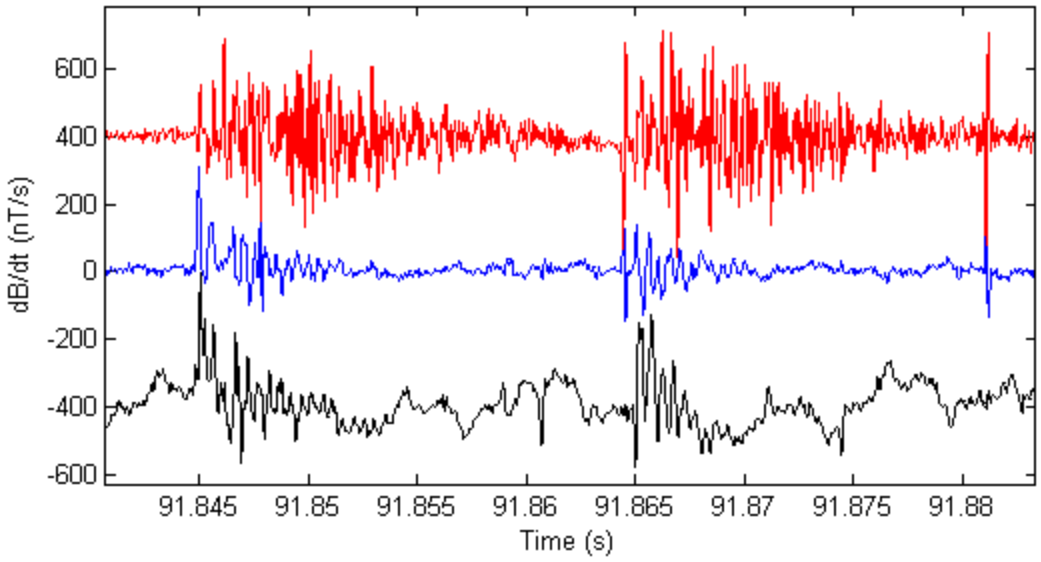

(b)

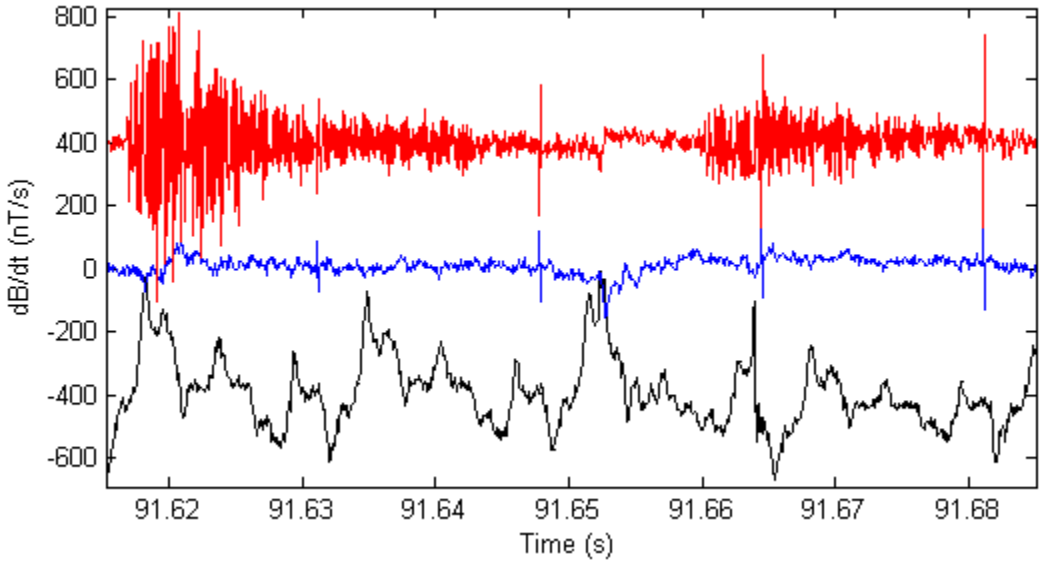

(c)

Figure 22. Temporal gradient applied to all three coil orientations for a section of sample A4 data; (a) The data for the x (northward) coil orientation is shown in red, y (eastward) coil orientation in blue, and z (vertical) coil orientation in black. The green area shown in detail in (b) has magnetic signals of interest in all three orientations, as opposed to (c) where magnetic signals of interest only appear in the x orientation.

It may be possible that these signals are amplified in some asymmetric way by the load frame. The frequency, time domain, and temporal gradient content of all signals recorded in the x orientation appear similar with the only difference being their respective amplitudes. Of the signals present in the y and z orientations, these also have consistent frequency spectra, time series and temporal derivatives. The reason that sometimes these signals are missing completely is unknown. The timing and correlation of the signal with audible fracturing does however suggest a consistent precursor which should be further explored with accelerometer, strain, acoustic and electric measurement systems in an attempt to locate its origin. The directional nature of the measurements is not clear and warrants further studies to map the field direction and strength in more detail.

The number of magnetic signals of interest found for the x-coil orientation for every sample type is listed in Table 1. The x and z components were not analyzed due to lack of time and perceived benefit.

Sample Number	Rock Type	Pressure at Failure (MPa)	Uniaxial Compressive Strength (MPa)	Number of Magnetic Signals of Interest	Total Difference (Maximum) Between Peaks (nT)
A1	Hb-Bi-Granite	18.6	139.8	N/A	N/A
A2	Hb-Bi-Granite	17.9	129.8	12	3.9576
A3	Hb-Bi-Granite	23.4	170.0	8	9.2374
A4	Hb-Bi-Granite	20.7	149.9	14	4.9089
B1	Hb-Bi-Qtz-Monzodiorite	17.2	124.2	11	6.9549
B2	Hb-Bi-Qtz-Monzodiorite	19.3	139.1	8	6.286
C1	Hb-Bi-Px-Po-Norite	24.1	172.3	4	9.5135
C2	Hb-Bi-Px-Po-Norite	24.1	172.3	3	7.9068
D1	Bi-Hb-Tonalite	24.1	172.6	5	8.4008
D2	Bi-Hb-Tonalite	17.2	123.1	4	5.5562
E1	Bi-Hb-Tonalite	20.0	142.7	2	9.6026
E2	Bi-Hb-Tonalite	16.5	117.8	5	6.7029
E3	Bi-Hb-Tonalite	21.4	152.3	4	9.5401
E4	Bi-Hb-Tonalite	18.6	132.9	4	8.3641
F1	Marble	9.7	57.6	0	7.3661
F2	Marble	9.7	57.7	3	4.95348
F3	Marble	9.7	57.2	9	5.3312
F4	Marble	8.3	49.6	0	1.24023
G1	Hb-Px-Mafic Dyke	24.8	241.1	11	4.7968
G2	Hb-Px-Mafic Dyke	24.1	234.6	13	9.8118
G6	Hb-Px-Mafic Dyke	22.8	221.3	11	9.6302
G7	Hb-Px-Mafic Dyke	14.5	140.7	4	4.57923
H1	Bi-Hb-Qtz-Monzodiorite	13.8	166.4	3	7.9486
H2	Bi-Hb-Qtz-Monzodiorite	17.2	207.9	4	7.0314
I1	Hb-Bi-Po-Norite	10.3	128.3	6	6.6845
I2	Hb-Bi-Po-Norite	10.3	128.5	5	5.46193
J1	Bi-Plagioclase-Gneiss	13.8	168.0	8	4.8765
J2	Bi-Plagioclase-Gneiss	17.2	209.9	6	9.0767
K1	Epidote-Qtz-Alkali Feldspar-Syenite	17.9	217.3	10	4.8682
K2	Epidote-Qtz-Alkali Feldspar-Syenite	24.8	300.5	4	9.7307
L1	Bi-Pyrite-Syenite	13.8	173.0	5	6.7117
L2	Bi-Pyrite-Syenite	14.5	180.9	5	7.3352

Table 1. Rock failure properties.

A brief study was completed to determine if there is any correlation between the number of magnetic signals of interest or the difference between peaks (the amplitude difference between the negative peak and the positive peak at failure) and any other properties listed in Table 1 and Table 2. The correlations were made with 1) the total difference between peaks 2) axial compressive strength, 3) pressure at failure, 4) number of signals of interest, 5) plagioclase and alkali feldspar percentage, and 6) plagioclase, alkali feldspar and pyroxene percentage. Of all the possible correlations examined, signals of interest vs. plagioclase, alkali feldspar, and pyroxene percentage was the only comparison which seemed to show any kind of correlation (Figure 23). This is interesting as these are the only three minerals in the samples that contain two cleavage planes at approximately 90 degrees; it is unknown if this is mere coincidence. These particular minerals were examined because Cress (1987) reported frequency responses in basalt, similar to those in granites, and marble, and Takeuchi (2005) and Freund (2006) reported electric current responses in gabbro and anorthosite up to 200 times stronger than other samples which were quartz rich. Note that the marble samples (red circles) do not follow the trend. Total difference between peaks vs. pressure at failure, and total difference between peaks vs. signals of interest also seemed to show slight correlation. These figures and the remaining correlation graphs can be found in Figure 32 (a) - (f), of Appendix E.

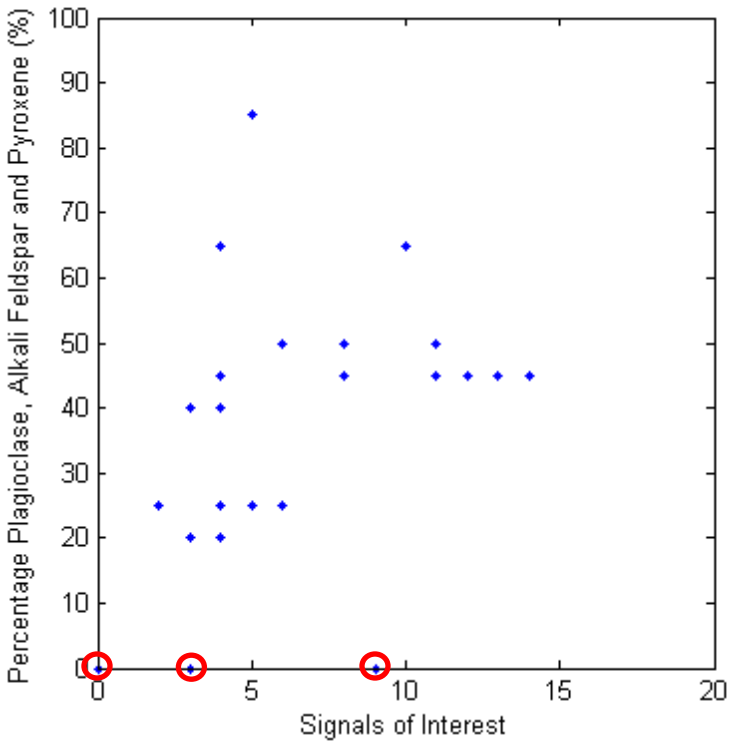

Figure 23. Correlation between signals of interest and plagioclase, alkali feldspar and pyroxene percentage. Marble samples are circled in red and do not follow the trend.

3.2.9 Future Work on Magnetic Data

Further research can be carried out on the datasets from the magnetic test. The majority of the analysis completed for this thesis focused on only the x-coil orientation. As mentioned in Section 3.2.8, signals of interest showed up most consistently and strongest in the x-coil orientation. All signals of interest in the remaining two orientations could be identified, and quantified. This would allow a comparison of the signals across all three coil orientations. With this information it may be possible to complete a vector analysis on the signals from the three orientations, the known coil orientations and locations, and pinpoint the sites and positioning of

the generation points of the signals of interest. With this information it may be easier to understand the cause of these signals.

Data surrounding the load frame collected at an acquisition frequency of 32 kHz was never successfully resampled to 9 kHz, the rate of data acquisition at the base station. Successful subtraction of the datasets could potentially lower the background noise field revealing further signals of interest. The difficulty in the time-matching of the two datasets was a result of the sampling method used by the program from which data was uncompressed and exported for analysis. Further work is required to first, understand completely the exportation process, and then alignment and subtraction of the data. A preliminary program, which saw limited success, was written in an attempt to accomplish this.

Further research should also be completed on some of the other signals found in the dataset, and mentioned in Section 3.2.8. Although identified, minimal analysis was completed on these signals to determine if any are a result of strain related events.

A general anomaly analysis program was also started for the purpose of classifying all anomalous signals in the x-coil orientation. This analysis should be completed and modified to run a similar analysis on all three coil orientations. By running filtering and smoothing algorithms, a slowly varying average of the magnetic dataset was created. Then by subtracting the magnetic data from this calculated average result, only anomalous signals remained for further classification. Classification of these anomalous signals into various sub groups, depending on properties, may allow the identification and characterization of further strain related events. One such example is pulsing in the number of events, which did not seem to correlate with pumping or failure as seen in Figure 24.

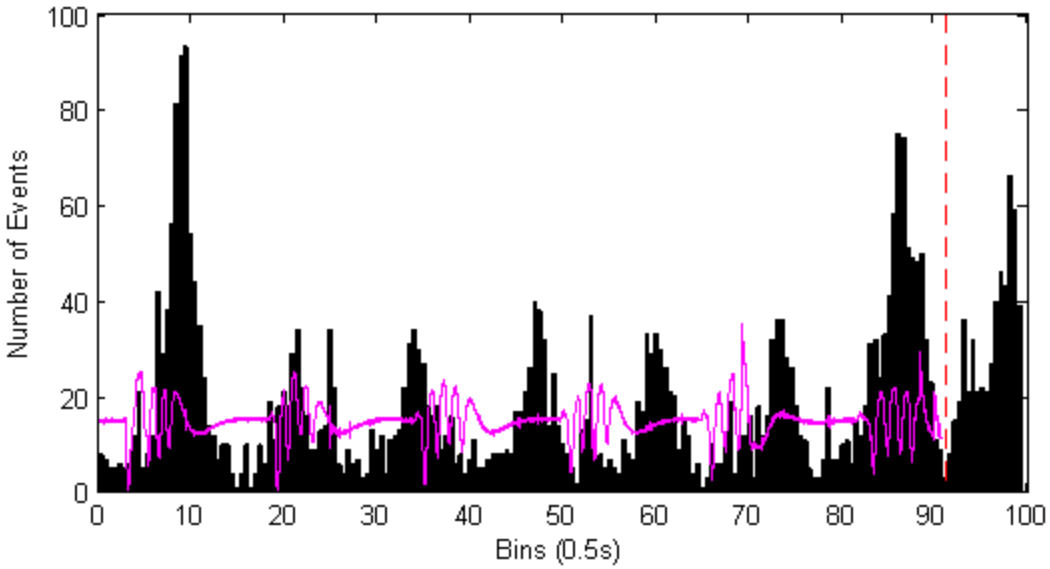

Figure 24. All anomalous signals found in the z-coil orientation for sample A4. The magenta line is the scaled data from which the analysis was completed to clearly show oscillating pumping every 10 s. The red dashed line signifies sample failure. It is clear that the number of anomalous events (black) in the data does not correlate with pumping (oscillations in magenta line), but may potentially correspond with the onset of pumping and failure. Similar, but less evident, pulsating of anomalous events occurs in all three coil orientations.

3.3 Future Follow up Experiments to Above Ground Magnetic Test

Further testing could be carried out underground to determine if there is the potential for measuring in an underground environment, similar signals to those identified. Before conducting such an underground experiment, further above ground measurements should be completed to become familiar with, and optimise, the data acquisition equipment, in an electromagnetic-noise-reduced environment.

Stressing rock in a controlled manner is difficult outside of the laboratory, so no emphasis should be placed on measuring strain related signals during further above-ground tests. The experiment should focus on baseline measurements with both magnetic coils and an electric system. As well the ground at the test site could be seismically stimulated using a sledge hammer to monitor the effects of ground motion on the instruments as it is not possible to completely uncouple the measurement systems from the ground. Understanding signals related to ground motion will allow an understanding of their impact in future underground experiments.

The above ground tests can be used in the design of a final underground experiment consisting of optimised collection techniques for identifying strain related signals underground. The optimal underground location would be a deep mine, as generally stress increases with depth. The more documentation available regarding cage movement, ventilation cycles, and sump pump patterns, the easier it will be to identify different sources of signal (or noise) in the data. Electromagnetic, acoustic, and seismic noise will be evident within the data, and therefore, being able to easily identify signals associated with mine infrastructure and mine operations is important. The area will require a 75 m borehole for an electric measurement system. The optimum measurement period would include at least one blast which could be used as a controlled experiment for measuring signals resulting from the seismoelectric effect. The seismic detectors should be selected so as to collect high-frequency information. This would allow seismic signals associated with cracking to be detected. As an alternative, microphones could also be attached to the rock and the signals recorded digitally using the same data acquisition systems.

Throughout both the above and underground experiments a magnetic base station should be set up at an above ground location in a low-noise environment. The base station data can be used for subtracting (or identifying) high-frequency sferic noise from underground datasets and will

also provide baseline noise measurements throughout the entire experimental period. Sferic noise can also be used to correlate datasets in the case of any time stamping failure. The level and effect of sferics on electric and magnetic data collection in a mine could also be determined.

4 Conclusions

Rockbursts are regular occurrences in deep mining environments around the world. Their frequency, unpredictable nature, and sometimes fatal consequences, means that it is important for mine safety to be able to identify locations where there are increases in strain, so the risk can be mitigated.

Electric and magnetic data collected over a period of five days from Coleman Mine, Sudbury Ontario, was analysed, however no stress or strain related signals were identified in the datasets. This is due mainly to having too many geophysical instruments running concurrently, and a lack of documentation regarding mining activity in the area to help with identifying various signals found in the data. The Coleman analyses lead to the development of a multi-part experiment.

The first part of the experiment was completed outdoors in a parking lot. A total of thirty-two samples, consisting of eleven different lithologies, were stressed until failure using a load frame. Magnetic coils located around the load frame were used to measure any potential magnetic fields induced when the core was stressed. Distinct and measurable magnetic signals associated with audible cracking for most rock samples, as well as consistent magnetic signals across all samples prior to failure were found. These signals might be amplified by the load frame in some way, so testing is required in an environment where rocks are stressed to cracking without a load frame (e,g. in a mine).

A correlation between the number of signals of interest and the percentage of plagioclase, alkali feldspar, and pyroxene appears from the data. This is unexpected, as quartz is a strongly

piezoelectric material and strong signals were expected from quartz rich rock. A larger sample suit is required to confirm these results.

The laboratory measurements should be followed up by above-ground field measurements prior to a carefully planned, passive acquisition, underground test. Successful identification of signals due to strain through these experiment could potentially prove the feasibility of a real-time underground geophysical monitoring system to improve safety.

5 References

Archibald, J. F., and P. A. Dirige, 2006, Developement of thin, spray-on liner and composite superliner area supports for damage mitigation in blast- and rock-induced rock failure events: Presented at the Ninth International Conference on Structures Under Shock and Impact (SUSI 2006).

Brady, B. T., and G. A. Rowell, 1986, Laboratory investigation of the electrodynamics of rock fracture: Nature, 321, 488– 492.

Bordes, C., L. Jouniaux, S. Garambois, M. Dietrich, and JP. Pozzi, 2008, Evidence of the theoretically predicted seismo-magnetic conversion: Geophysical Journal International, 174 (2), 489-504.

Carpinteri, A., G. Lacidogna, O. Borla, A. Manuello, and G. Niccolini, 2012, Electromagnetic and neutron emissions from brittle rocks failure: Experimental evidence and geological implications: Sadhana, 37, 59–78.

Crampin, S., 2001, Developing stress-monitoring sites using cross-hole seismology to stress-forecast the times and magnitudes of future earthquakes: Tectonophysics, 338, 233–245.

Cress, G. O., B. T. Brady, and G. A. Rowell, 1987, Sources of electromagnetic radiation from fracture or rock samples in the laboratory: Geophysical Research Letters, vol. 40, no 4, 331-334.

Dazhao, S., W. Enyuan, W. Chao, and X. Fule, 2010, Electromagnetic radiation early warning criterion of rock burst based on statistical theory: Mining Science and Technology, 20, 0686–0690.

Dupuis, C., 2008, Field measurements and analysis of electrokinetic seismoelectric signals generated in sedimentary environments: PhD thesis, University of New Brunswick.

Fenoglio, M. A., M. J. S. Johnston, and J. D. Byerlee, 1995, Magnetic and electric fields associated with changes in high pore pressure in fault zones: Application to the Loma Prieta ULF emissions: Journal of Geophysical Research, vol. 100, no. B7, 12951–12958.

Freund, F., 2002, Charge generation and propagation in igneous rocks: Journal of Geodynamics, 33, 543–570.

Freund, F. T., A. Takeuchi, and B. W. Lau, 2006, Electric currents streaming out of stressed igneous rocks - a step towards understanding pre-earthquake low frequency EM emissions: Physics and Chemistry of the Earth, 31, 389–396.

Frid, V., 2000, Electromagnetic radiation method waterinfusion control in rockburst-prone strata: Journal of Applied Geophysics, 43, 5–13.

Frid, V., 2001, Calculation of electromagnetic radiation criterion for rockburst hazard forecast in coal mines: Pure and Applied Geophysics, 158, 931–944.

Frid, V., A. Rabinovitch, and D. Bahat, 2003, Fracture induced electromagnetic radiation: Journal of Physics D: Applied Physics, 36, 1620–1628.

Gershenzon, N., G. Bambakidis, and I. Temovskiy, 2014, Coseismic electromagnetic field due to the electrokinetic effect: Geophysics, vol. 79, no. 5, E217-E229.

Gokhberg, M. B., and V. A. Morgounov, 1982, Experimental measurements of electromagnetic emissions possibly related to earthquakes in Japan: Journal of Geophysical Research, 87, 7824–7828.

Goldbaum, J., V. Frid, D. Bahat, and A. Rabinovitch, 2003, An analysis of complex electromagnetic radiation signals induced by fracture: Measurement Science and Technology, 14, 1839–1844.

Greiling, R. O., and H. Obermeyer, 2010, Natural electromagnetic radiation (EMR) and its application in structural geology and neotectonics: Journal Geological Society of India, 75, 278–288.

Hui-lin, J., W. En-yuan, S. Xiao-yan, Z. Hong-jie, and L. Zhong-hui, 2009, Correlation of electromagnetic radiation emitted from coal or rock to supporting resistance: Mining Science and Technology, 19, 0317–0320.

Hutchinson, J., and M. Diederichs, 1996: *Cablebolting in underground mines*. Richmond, British Columbia: BiTech Publishers Ltd.

Ikeya, M., C. Yamanaka, T. Mattsuda, H. Sasaoka, H. Ochiai, Q. Huang, N. Ohtani, T. Komuranani, M. Ohta, Y. Ohno, and T. Nakagawa, 2000, Electromagnetic pulses generated by compression of granitic rocks and animal behavoir: Episodes, 23, 262–265.

Kepic, A., 1995, Seismoelectric responses from sulphide orebodies: PhD thesis, University of British Columbia.

Kepic, A., R. D. Russell, M. Maxwell, and K. E. Butler, 2001, Underground tests of the radio pulsed effect seismoelectric method at the Lynx Mine, Canada: Exploration Geophysics, 32, 107–112.

Krumbholz, M., 2010, Electromagnetic radiation as a tool to determine actual crustal stresses - applications and limitations: PhD thesis, Universitat zu Gottingen.

Lichtenberger, M., 2006, Underground measurements of electromagnetic radiation related to stress-induced fractures in the Odenwald Mountains (Germany): Pure Applied Geophysics, 163, 1661–1677.

Lin-Ming, D., L. Cai-ping, M. Zong-long, and G. Ming-shi, 2009, Prevention and forecasting of rock burst hazards in coal mines: Mining Science and Technology, 19, 0585–0591.

McNutt, S. R., 1996, Seismic monitoring and eruption forecasting of volcanoes: a review of the state-of-the-art and case studies: This document is included in the publication, *Monitoring and Mitigation of Volcano Hazards, R. Scarpa and R. Tilling (eds.)*, published by Springer-Verlag, Berlin, Heidelberg, on behalf of the Alaska Volcano Observatory, Geophysical Institute, University of Alaska Fairbanks, 99–146 .

Mendecki, A., G. Van Aswegen, and P. Mountfort, 1999, This document is included as Chapter 9 of the publication, *A Handbook on Rock Engineering Practice for Tabular Hard Rock Mines, A. J. Jager and J. A. Ryder (eds.),* published by CredaCommunications, Cape Town, on behalf of the Safety in Mines Research Advisory Committee to the Department of Minerals and Energy of South Africa.

Mizutani, H., T. Ishido, T. Yokokura, and S. Ohnishi, 1976, Electrokinetic phenomena associated with earthquakes: Geophysical Research Letters, vol. 3, no. 7, 365-368.

Molchanov, O. A., and M. Hayakawa, 1998, On the generation mechanism of ULF seismogenic electromagnetic emissions: Physics of the Earth and Planetary Interiors, 105, 201–210.

Mori, Y., Y. Obata, and J. Sikula, 2009, Acoustic and electromagnetic emission from crack created in rock sample under deformation: Journal of Acoustic Emission, 27, 157–165.

Nitson, U., 1977, Electromagnetic emission accompanying fracture of quartz-bearing rocks: Geophysical Research Letters, vol. 4, no. 8, 333-336.

O'Keefe, S. G., and D. V. Thiel, 1991, Electromagnetic emissions during rock blasting: Geophysical Research Letters, vol. 18, no. 5, 889–892.

Pun, W., 2011, Geophysical time series data from a stressed environment: Master's thesis, University of Toronto.

Sedlak, V., 1997, Energy evaluation of de-stress blasting: Acta Montanistica Slovaca, 2, 11–15.

Sjöberg, J., R. Christiansson, and J. A. Hudson, 2003, ISRM suggested methods for rock stress estimation – Part 2: overcoring methods: International Journal of Rock Mechanics and Mining Sciences, 40, 999–1010.

Smith, A. C. F., A. Bernardi, P. R. McGill, M. E. Ladd, R. A. Helliwell, and O. G. V. Jr, 1990, Low frequency magnetic field measurements near the epicenter of the ms 7.1 Loma Prieta earthquake: Geophysical Research Letters, 17, 1465–1468.

Takeuchi, A., B. W. S. Lau, and F. T. Freund, 2005, Current and surface potentials induced by stress-activated positive holes in igneous rocks: in Physics and Chemistry of the Earth, 31, 240 – 247.

Triantis, D., C. Anastasiadis, and I. Stavrakas, 2008, The correlation of electrical charge with strain on stressed rock samples: Natural Hazards and Earth System Sciences, 8, 1243–1248.

Vallianatos, F., and D. Triantis, 2008, Scaling in pressure stimulated currents related with rock fracture: Physica A, 387, 4940–4946.

Wan, G., X. Li, and L. Hong, 2008, Piezoelectric response of brittle rock mass containing quartz to static stress and exploding stress wave respectively: Journal of Central South University of Technology, 15, 344–349.

Wang, E., X. He, L. Dou, S. Zhou, B. Nie, and Z. Liu, 2005, Characteristics of electromagnetic radiation from coal or rock during excavation and their applications: Chinese Journal of Geophysics, vol. 48, no. 1, 237-242.

Werner-Allen, G., J. Johnson, M. Ruiz, J. Lees, and M. Welsh, 2005, Monitoring volcanic eruptions with wireless sensor network. In Proc. Second European Workshop on Wireless Sensor Networks (EWSN'05).

Xu, J., F. Ma, and J. Han, 2012, Rockburst hazard assessment based on electromagnetic emission in Xingfu Mine: Journal of Coal Science and Engineering, vol. 18,no 1, 25–28.

Xuequi, H., N. Baisheng, C. Wenxue, W. Enyuan, D. Linming, W. Yunhai, L. Mingju, and H. Mitri, 2012, Research progress on electromagnetic radiation in gas-containing coal and rock fracture and it's applications: Safety Science, 50, 728–735.

Yoshida, S., O. C. Clint, and P. R. Sammonds, 1998, Electric potential changes prior to shear fracture in dry and saturated rocks: Geophysical Research Letters, 25, 1577–1580.

Yoshida, S., and T. Ogawa, 2004, Electromagnetic emissions from dry and wet granite associated with acoustic emissions: Journal of Geophysical Research, 109.

Yoshida, S., M. Uyeshima, and M. Nakatani, 1997, Electric potential changes associated with slip failure of granite: Preseismic and coseismic signals: Journal of Geophysical Research, 102, 14883–14897.

Zhu, Z., S. Chi, X. Zhan, and M. N. Toksoz, 2008, Theoretical and experimental studies of seismoelectric conversions in boreholes: Communications in Computational Physics, vol. 3, no 1, 109–120.

Appendix A: Description of algorithms for analysis of Coleman Mine data

Electric data from Coleman mine was first processed to remove the voltage response from current injection. The injection pattern consisted of 168 different electrode configurations, repeating throughout the 4 day collection period. As the curves seen in Figure 4 varied slightly for various electrode configurations, and due to evaporation of the water in the surface and bore-holes throughout the measurement period, a unique analysis had to be completed for the four curves collected on each day. The general shape of the curves remaining the same allowed the averaging of curves produced from the same sequence of current injections. Upon averaging, the curves were smoothed to eliminate any high frequency variations. The average curves were normalized to the curves resulting from the respective current injection patterns and then subtracted. After subtraction only the additional signals should remain.

Magnetic data from Coleman mine was initially processed with an algorithm to remove 60 Hz noise. As the width and amplitude of the 60 Hz peak and respective harmonics varied slightly with time, the algorithm located the peaks in frequency domain and determined their widths before removing them with notch filters. The algorithm which identified anomalies worked on data from which low-frequency signal (e.g. drift) had been removed using a smoothing function that ignored outliers. Using various parameters of frequency (described below), amplitude, duration, and speed of onset/decay, all anomalies remaining were binned with information on the location of the signal in the data and the raw anomaly before subtraction of the smoothed data.

Frequency as a function of time was calculated for the entire magnetic dataset at various levels of detail using an algorithm which implemented a sliding Fourier transform. Depending on the detail required (small/large scale), the number of data points that were included in the Fourier transforms was varied. Small scale variation frequency analysis was implemented for

determining the frequency characteristic content of individual anomalies as mentioned previously.

An algorithm was written to identify signals due to seismic motion as this was potentially valuable for analysis of the seismo-electric/magnetic effect in the magnetic data. As the time stamping in either or both of the magnetic and seismic datasets is incorrect, it was not possible to correlate the known seismic events with the anomalies in the other datasets.

Appendix B: Unsuccessful analysis completed on Coleman Mine data

In addition to the work already discussed in Section 3.1, the remainder of analysis completed on the Coleman Mine electric and magnetic datasets will be discussed.

Magnetic data was presented with arbitrary units throughout the document due to the instrument gains being unknown. An attempt was made to calibrate the magnitude of the magnetic field from the known injected current from the electric experiment recorded with the magnetic antennas. It was found that regardless of the current electrodes used for injection, the magnetic response did not have an amplitude that behaved in a predictable manner with the separation between the electrode pair and the magnetic antenna. It is assumed that one or more of the current carrying wires that supplied the electrodes were lying near the magnetic antennas. The unknown proximity of this wire means magnetic response could not be accurately estimated. In addition, comparison of electric and magnetic datasets found that magnetic data was $d\vec{B}/dt$ rather than $\vec{B}$.

This analysis also suggests that evaporation of water in surface and borehole electrodes, resulted in poor contact, and that this resulted in drift, poor and anomalous readings, and the occasional failure to complete a reading.

A frequency as a function of time analysis was completed on the electric data, as for magnetic. The results were mixed, with some evidence of 60 Hz power line noise. Similar filters as to the magnetic data were applied to the electric data; however results pertaining to strain related signals were still inconclusive.

Although only briefly mentioned in this document previously, significant attempts were made to compare and align all datasets. Electric and magnetic datasets were aligned as the magnetic field associated with the current injection was evident in the magnetic data. Because an approximate

start time was recorded for each time the current injection system was switched on (6 times), approximate time stamping could be added to the magnetic data confirming that the included time stamp was incorrect. Attempting to correlate the seismic data with the magnetic and electric data was never successful.

Data from the two magnetic coils located approximately 30 m apart was also compared to see if slowly varying and common signals could be removed via subtraction of the two dataset, with the remaining signals being considered to occur in closer proximity to one of the magnetic coils. The process never successfully removed the most obvious signals, from the current injection, even after applying a scaling to data, and was therefore considered ineffective, as no sense could be made of the results.

Appendix C: Rock Sample Properties

Sample Number	Rock Type	Depth Retrieved From (m)	Sample Length and Diameter (cm)	Percentage Quartz (%)	Percentage Plagioclase (%)	Percentage Alkali Feldspar (%)	Percentage Mafic or Other (%)	Grain Size
A1	Hb-Bi-Granite	457	10.5/4.7	50	40	<5	10	Course
A2	Hb-Bi-Granite	457	10.4/4.7	50	40	<5	10	Course
A3	Hb-Bi-Granite	457	10.5/4.7	50	40	<5	10	Course
A4	Hb-Bi-Granite	457	10.4/4.7	50	40	<5	10	Course
B1	Hb-Bi-Qtz-Monzodiorite	453	10.4/4.7	10	10	40	40	Course
B2	Hb-Bi-Qtz-Monzodiorite	453	10.4/4.7	10	10	40	40	Course
C1	Hb-Bi-Px-Po-Norite	96	10.5/4.8	0	0	5	90 5 Pyrrhotite	Med.
C2	Hb-Bi-Px-Po-Norite	96	10.5/4.7	0	0	5	90 5 Pyrrhotite	Med.
D1	Bi-Hb-Tonalite	Unknown	10.5/4.7	15	25	0	60 <5 Epidote	Med. - Course
D2	Bi-Hb-Tonalite	Unknown	10.3/4.8	15	25	0	60 <5 Epidote	Med. - Course
E1	Bi-Hb-Tonalite	Unknown	10.4/4.8	15	25	0	60 <5 Epidote	Med. - Course
E2	Bi-Hb-Tonalite	Unknown	10.4/4.8	15	25	0	60 <5 Epidote	Med. - Course
E3	Bi-Hb-Tonalite	Unknown	10.4/4.8	15	25	0	60 <5 Epidote	Med. - Course
E4	Bi-Hb-Tonalit	Unknown	10.4/4.8	15	25	0	60 <5	Med. - Course

	e						Epidote	
F1	Marble	Unknown	13.0/5.2	0	0	0	No Inclusions	Med.
F2	Marble	Unknown	13.0/5.2	0	0	0	No Inclusions	Med.
F3	Marble	Unknown	13.2/5.2	0	0	0	No Inclusions	Med.
F4	Marble	Unknown	13.1/5.1	0	0	0	No Inclusions	Med.
G1	Hb-Px-Mafic Dyke	Unknown	10.4/4.1	0	5	0	95	Fine
G2	Hb-Px-Mafic Dyke	Unknown	10.4/4.1	0	5	0	95	Fine
G6	Hb-Px-Mafic Dyke	Unknown	10.5/4.1	0	5	0	95	Fine
G7	Hb-Px-Mafic Dyke	Unknown	10.4/4.1	0	5	0	95	Fine
H1	Bi-Hb-Qtz-Monzo diorite	Unknown	10.2/3.7	15	30	10	45	Course
H2	Bi-Hb-Qtz-Monzo diorite	Unknown	10.4/3.7	15	30	10	45	Course
I1	Hb-Bi-Po-Norite	Unknown	10.5/3.6	0	25	0	70 5 Pyrrhotite <5 Epidote	Course
I2	Hb-Bi-Po-Norite	Unknown	10.4/3.6	0	25	0	70 5 Pyrrhotite <5 Epidote	Course
J1	Bi-Plagioclase-Gneiss	Unknown	10.4/3.6	0	50	0	50	Med.
J2	Bi-Plagioclase-	Unknown	10.4/3.6	0	50	0	50	Med.

	Gneiss							
K1	Epidote -Qtz- Alkali Feldspar- Syenite	Unknown	10.3/3.6	15	0	65	20 Epidote	Course
K2	Epidote -Qtz- Alkali Feldspar- Syenite	Unknown	10.4/3.6	15	0	65	20 Epidote	Course
L1	Bi- Pyrite- Syenite	Unknown	10.4/3.6	0	15	75	10 <5 pyrite	Med. - Course
L2	Bi- Pyrite- Syenite	Unknown	10.4/3.6	0	15	75	10 <5 pyrite	Med. - Course

Table 2. Each rock types respective location and depth recovered from, length and diameter, mineralization and grain size. Mineralization was estimated from hand-samples pre-failure.

Appendix D: Description of algorithms for analysis of magnetic data from the load frame

Magnetic data collected from around the load frame utilized proprietary Vale software for initial analysis. It was found that using this software for elimination of 60 Hz and respective even and odd harmonic noise was more effective than a variation of the algorithm created for analysis of Coleman Mine magnetic data which eliminated larger portions of the data with notch filters.

Anomalous signals in the magnetic data were determined with the same method as for the Coleman Mine data, described in Appendix A.

An algorithm for frequency analysis as a function of time was applied to the data that was similar to the one applied to the Coleman Mine data. It was however found that accurate frequency data for specific anomalies could not be extracted due to the large variation in frequency content in certain signals, so a second function which executed fast Fourier transforms on a short section of the anomalous data was used, as well as a third function which calculated the approximate frequency of very short anomalous signals by determining the number of peaks and troughs in the signal.

Magnetic signals of interest could not be consistently and accurately identified from the time series data so a temporal derivative was applied. After the application of this derivative, algorithms were used to identify the length of an anomalous signal, its frequency, and initial amplitude after onset. The signals varied slightly from rock sample to rock sample: for example, some samples consistently had slightly lower onset amplitudes. Parameters could be adjusted to identify weaker anomalous signals, but this generally resulted in noise being identified. The frequency analysis described in Appendix E was found to be more successful at identifying anomalous signals associated with stress events.

Appendix E: The Picking of Signals of Interest and Other Common Signals

An algorithm containing a very general definition of the magnetic signals of interest was used for scanning the data and finding and counting events. Parameters were set so no signals of interest were excluded; however, this often resulted in the inclusion of many false picks. Shown below in Figure 25 - Figure 29 are some of the most common signals found throughout the datasets. Figure 25 and Figure 26 are examples of what are considered good picks, containing two frequency peaks between 4000 and 6000 Hz on the frequency spectra (panel c). A small number of the good picks also contained a frequency spike at 2000 Hz. Figure 27 through Figure 29 are the most common examples of false picks. Although the time-domain and temporal-derivative data often appears similar for some of these false picks, the frequency spectra generally shows a different signature. The occasional signal with subtle characteristics of a good pick such as that shown in Figure 29 would appear during the analysis. To avoid any bias in picking, an algorithm with stringent frequency properties was run on these signals to determine if their frequency peaks resembled the signals of interest sufficiently. The signal shown in Figure 29 failed this second analysis and was not included in the count of the signals of interest.

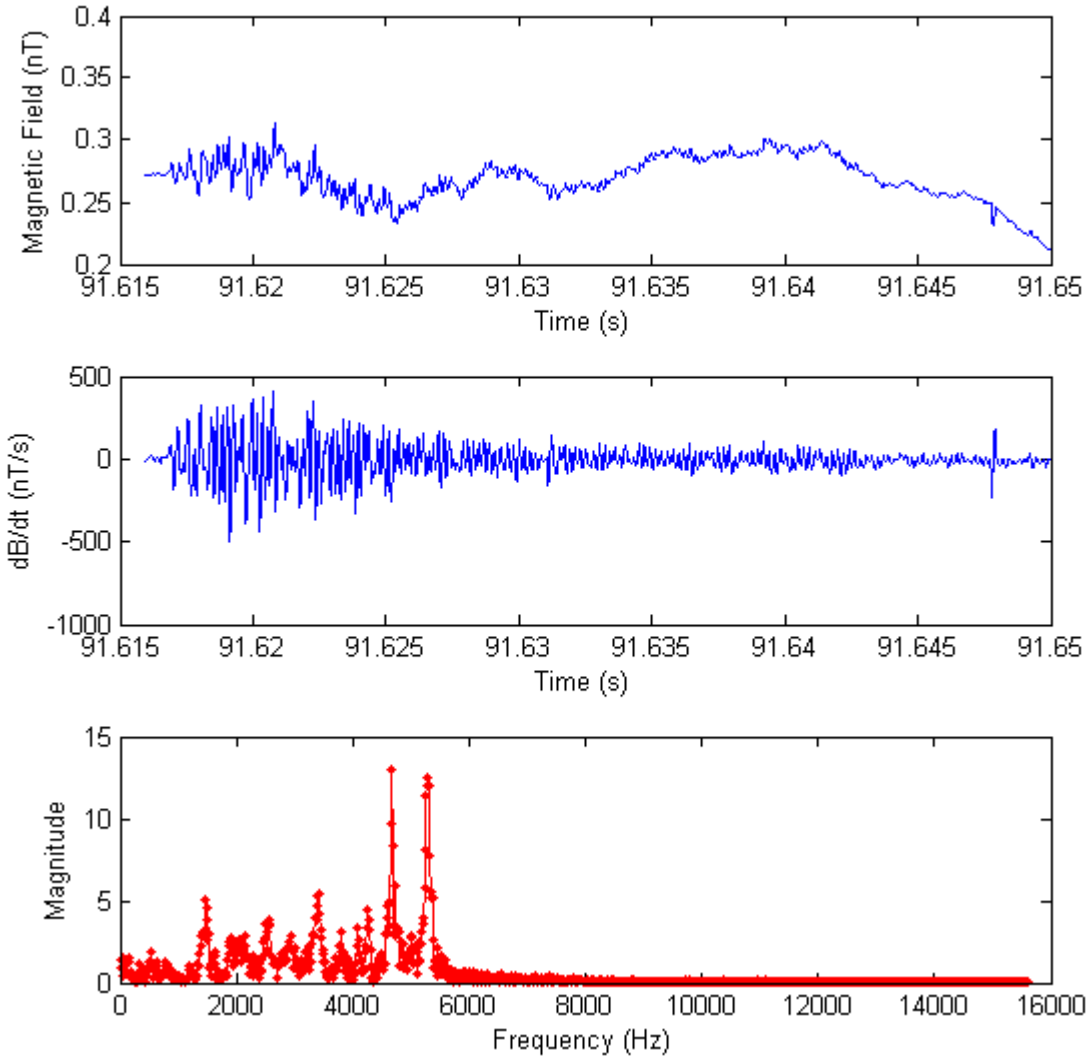

Figure 25. One of the magnetic signals of interest found when stressing Sample A4. The top panel is the magnetic field, the middle panel is the temporal gradient, and the bottom panel is the frequency spectrum of the temporal gradient. This is an example of a signal associated with cracking with the two well defined frequency spikes between 4000 and 5000 Hz.

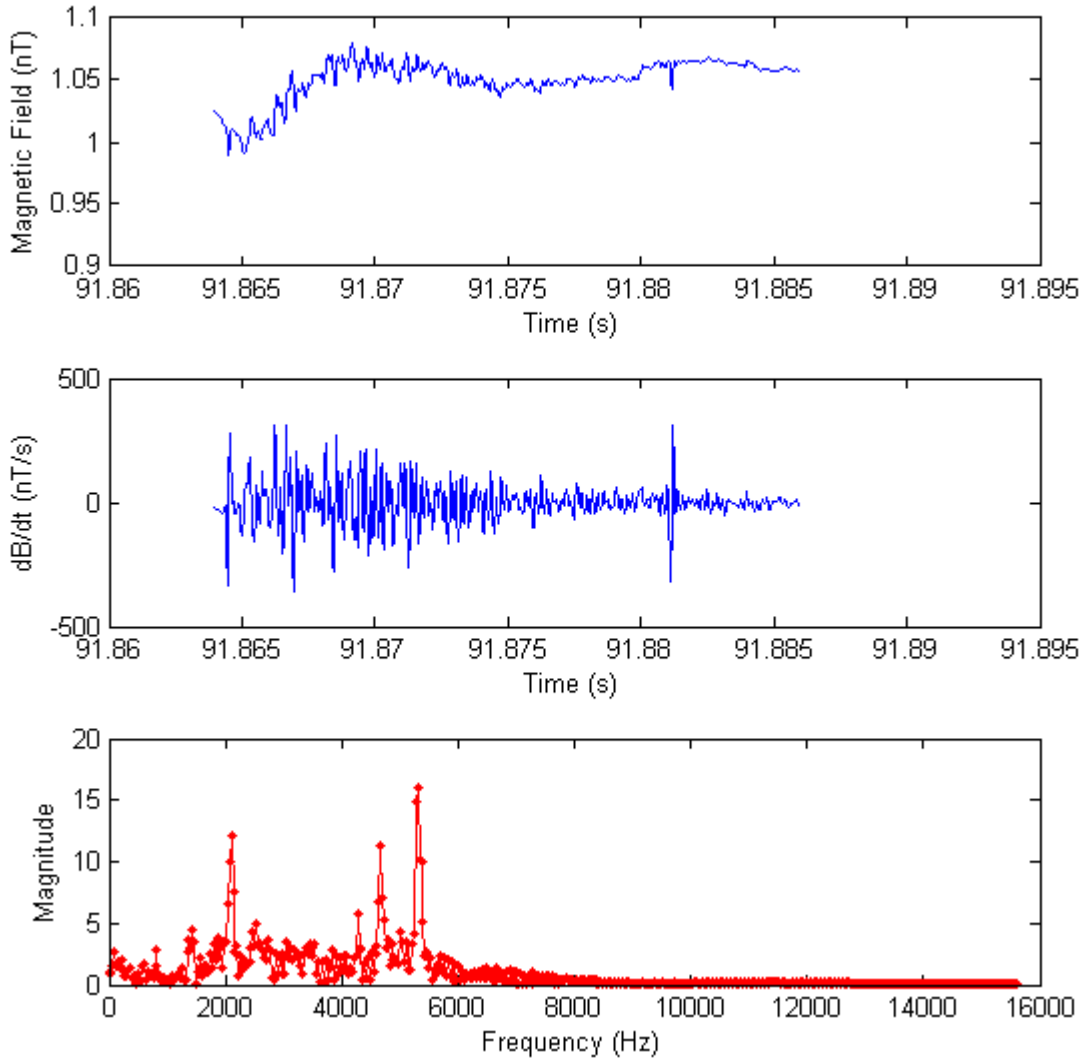

Figure 26. Another of the magnetic signals of interest found when stressing Sample A4. The top panel is the magnetic field, the middle panel is the temporal gradient, and the bottom panel is the frequency spectrum of the temporal gradient. This is an example of a signal associated with cracking with the two well defined frequency spikes between 4000 and 5000 Hz in addition to a frequency spike at 2000Hz.

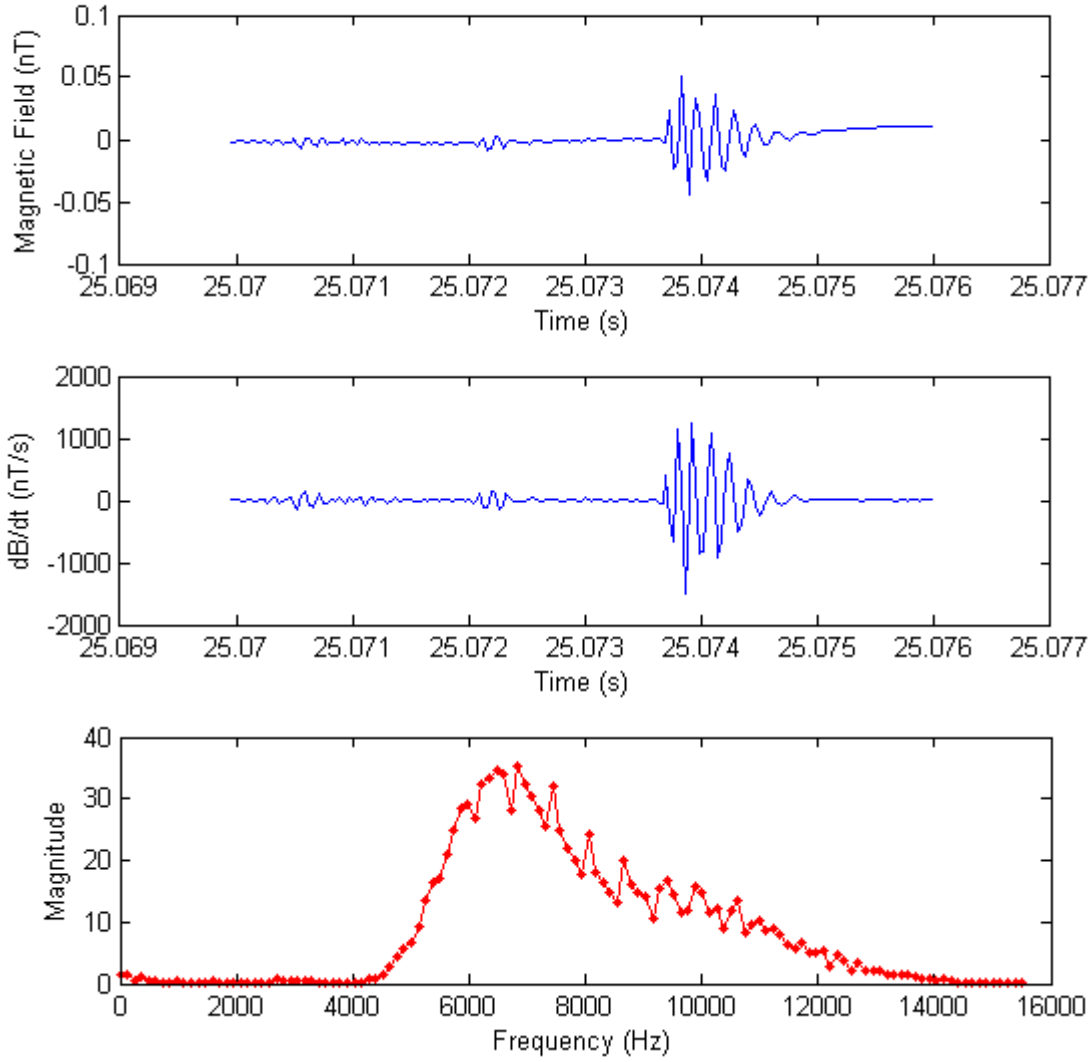

Figure 27. Magnetic signal found in Sample A4 and shown in Figure 18. The top panel is the magnetic field, the middle panel is the temporal gradient, and the bottom panel is the frequency spectrum of the temporal gradient. This is an example of an event not associated with audible cracking.

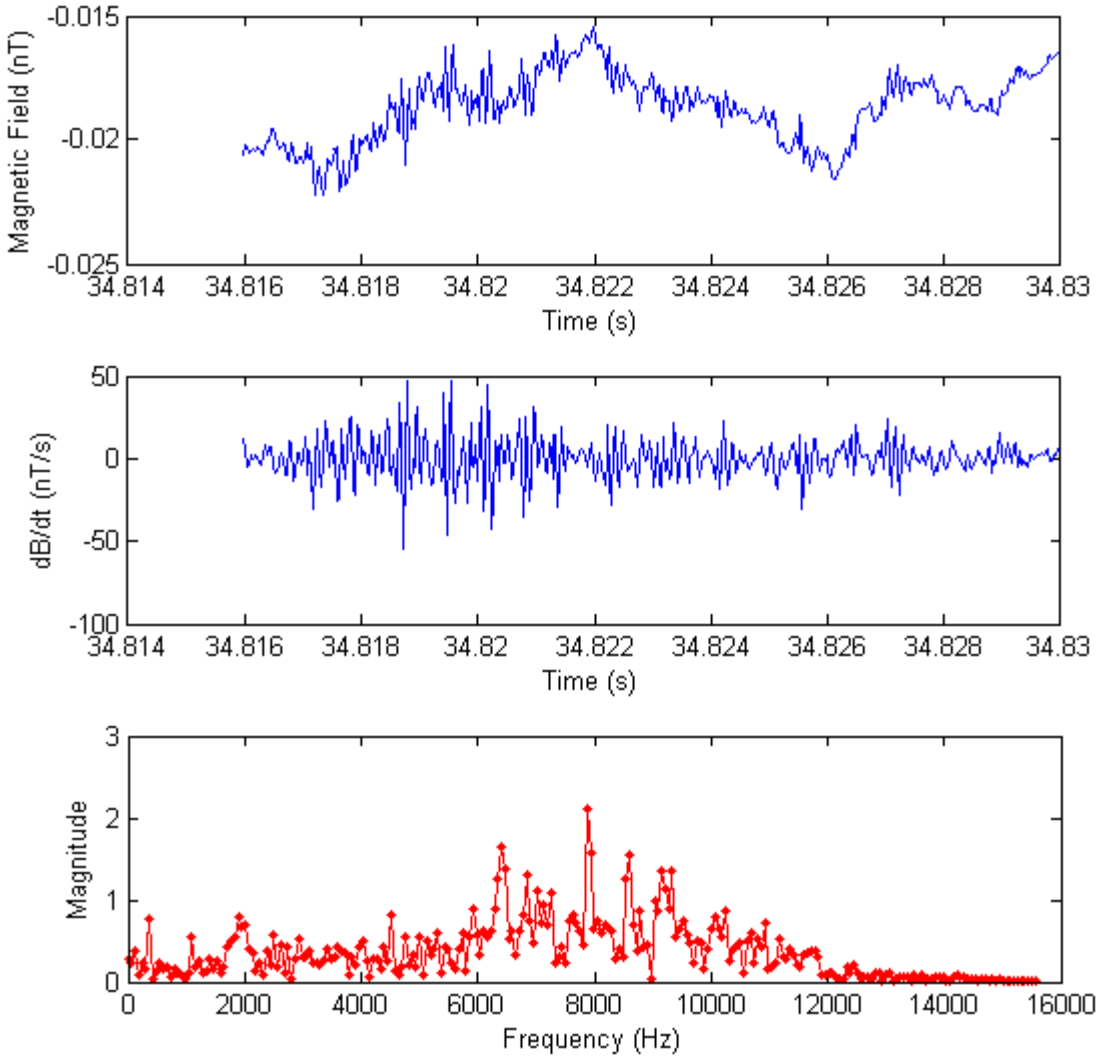

Figure 28. Magnetic signal generated when stressing Sample E3. The top panel is the magnetic field, the middle panel is the temporal gradient, and the bottom panel is the frequency spectrum of the temporal gradient. This is an example of an event not associated with audible cracking. The above signal represents the most common variety of these signals, as the temporal gradient signals resemble the properties of good picks. The frequency spectrum however differs, showing a broader high frequency trend.

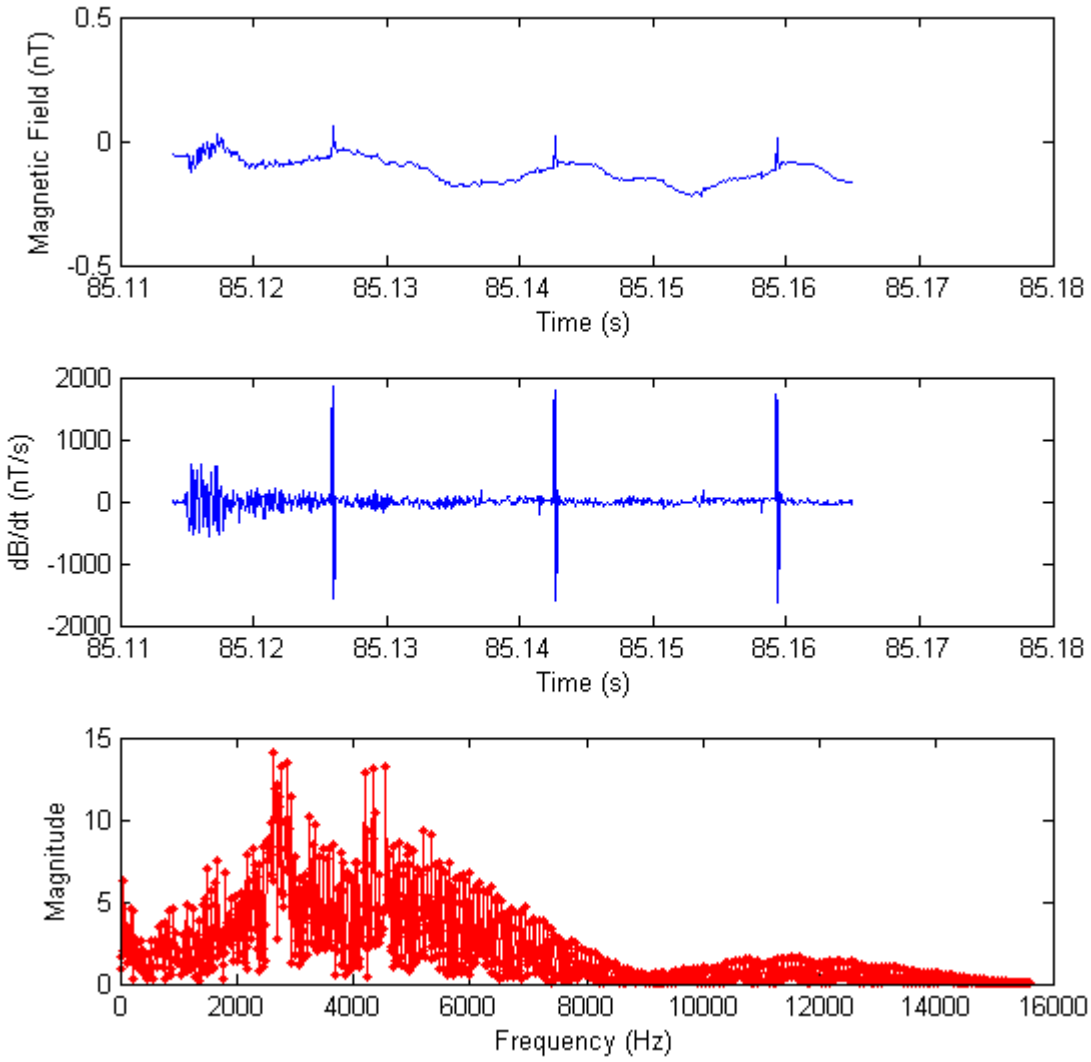

Figure 29. Another magnetic signal found when stressing sample E3. The top panel is the magnetic field, the middle panel is the temporal gradient, and the bottom panel is the frequency spectrum of the temporal gradient. This is an example of an event not associated with audible cracking; however there does appear to be frequency spikes between 4000 and 6000 Hz as well as near 2000 Hz. The above could be eliminated as magnetic signal of interest by a modified algorithm with more stringent frequency properties for picking.

Appendix F: Signals of Interest within Regions of Audible Cracking

For completeness, the temporal derivative time series for samples F3, A3, E3, E4, G6, and G7 are shown (Figure 30 (a) – (f)). Black arrows indicate magnetic signals of interest. Thicker black arrows are due to regions with multiple signals stacking on top of each other. As mentioned, these signals only appeared during audible cracking which are shown with vertical lines. Magenta lines indicate the onset of audible cracking, green lines their cessation. The final green line also indicates the moment of visible sample failure.

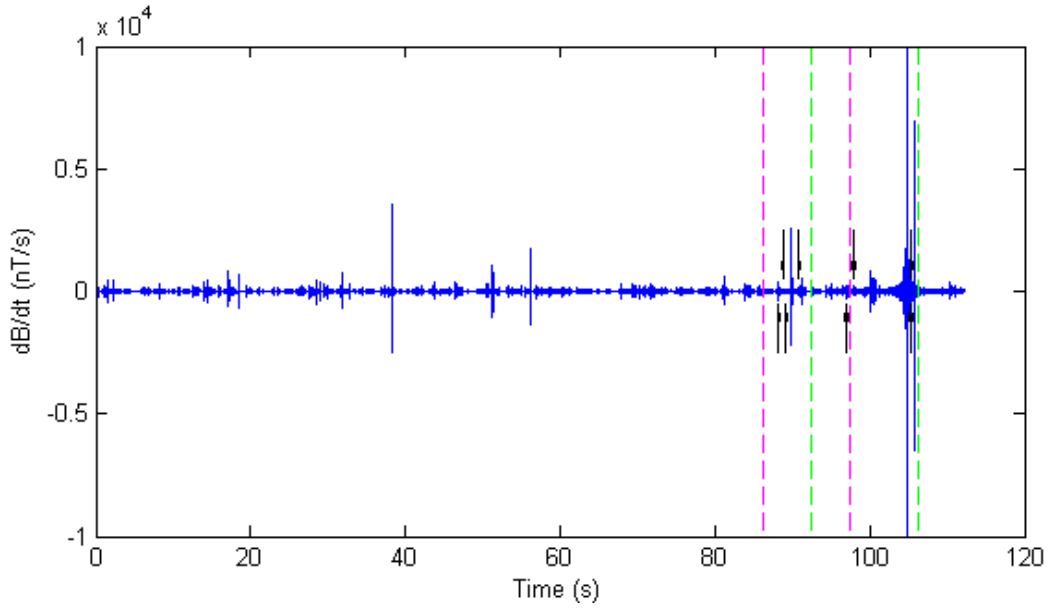

(a)

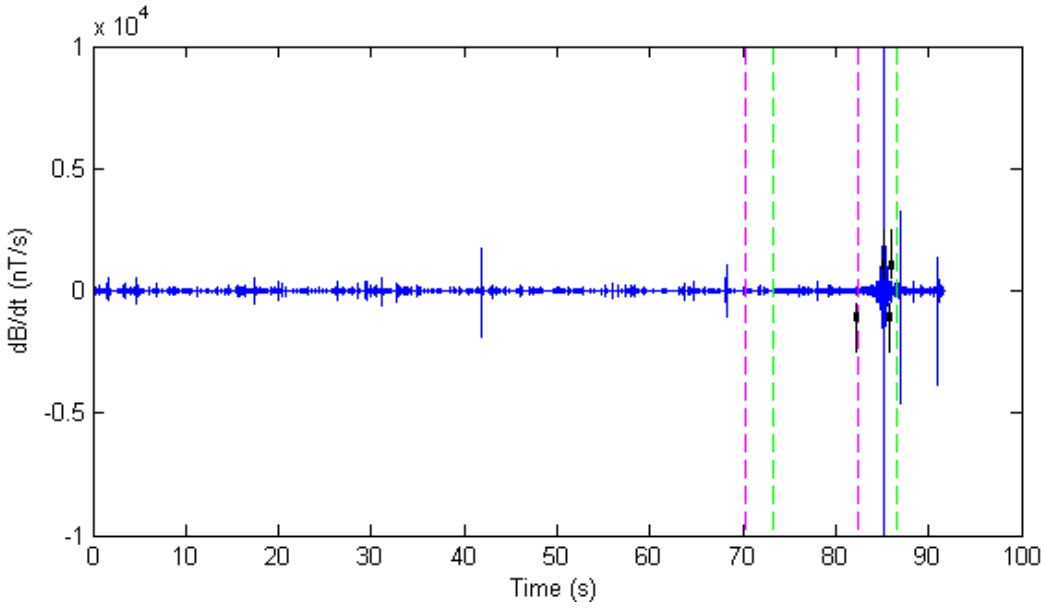
x 10^4
1
0.5
0
-0.5
-1
dB/dt (nT/s)
0
10
20
30
40
50
60
70
80
90
100
Time (s)

(b)

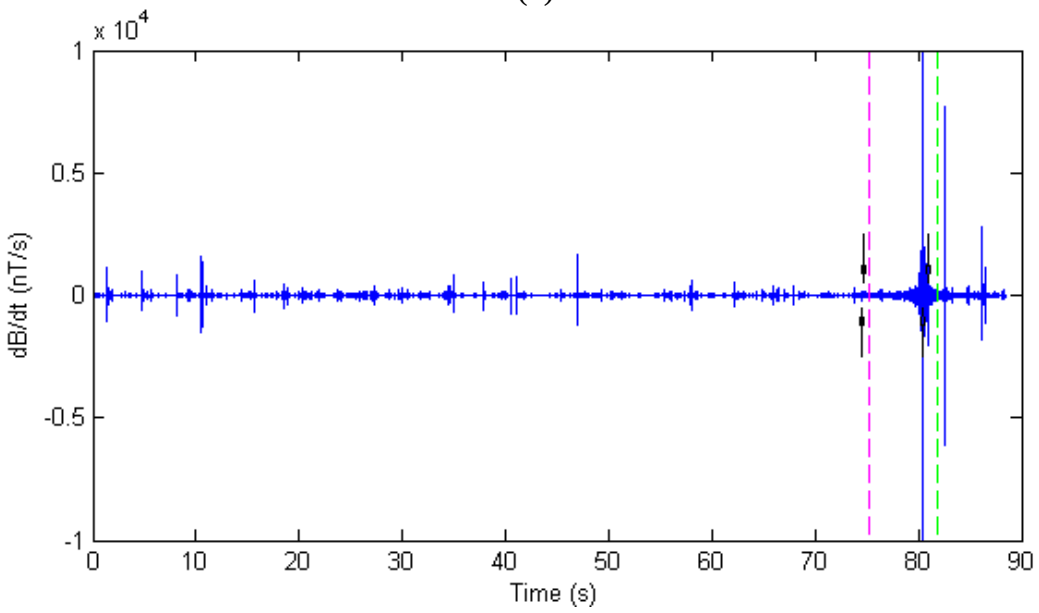
x 10^4
1
0.5
0
-0.5
-1
dB/dt (nT/s)
0
10
20
30
40
50
60
70
80
90
Time (s)

(c)

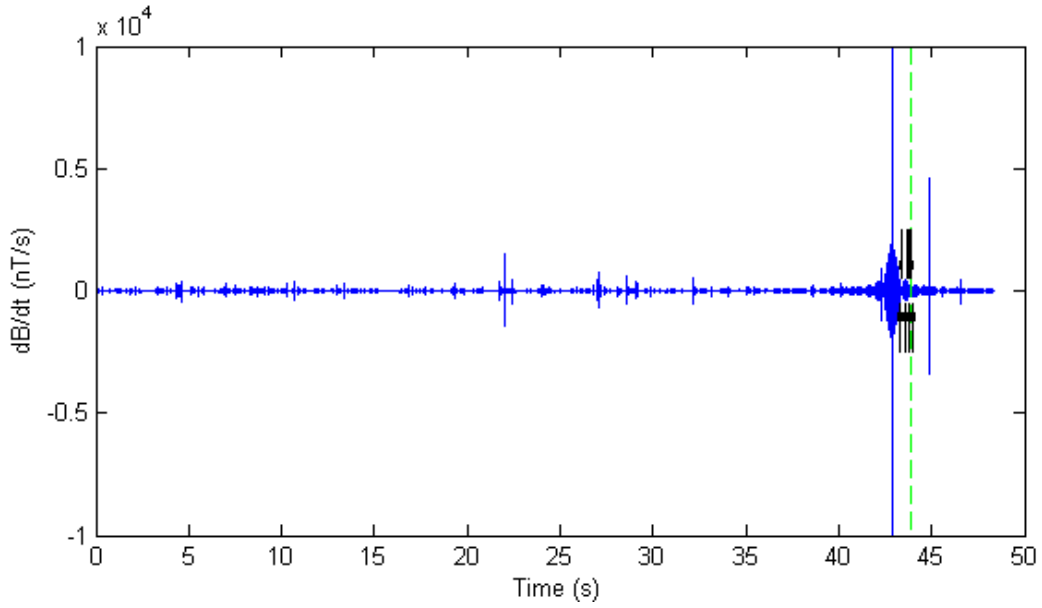
x 10^4
1
0.5
0
-0.5
-1
dB/dt (nT/s)
0
5
10
15
20
25
30
35
40
45
50
Time (s)

(d)

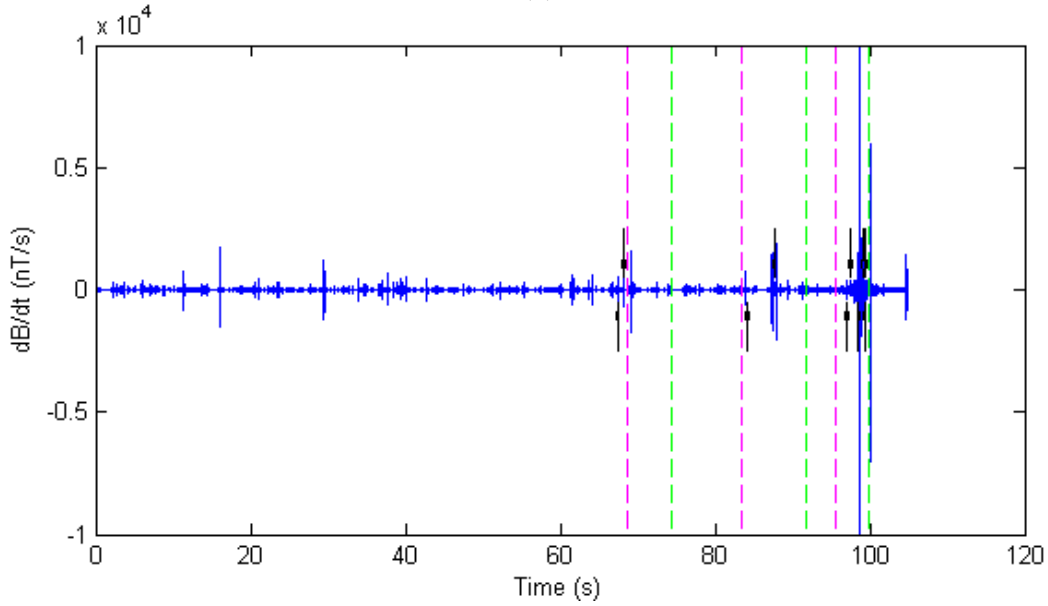
x 10^4
1
0.5
0
-0.5
-1
dB/dt (nT/s)
0
20
40
60
80
100
120
Time (s)

(e)

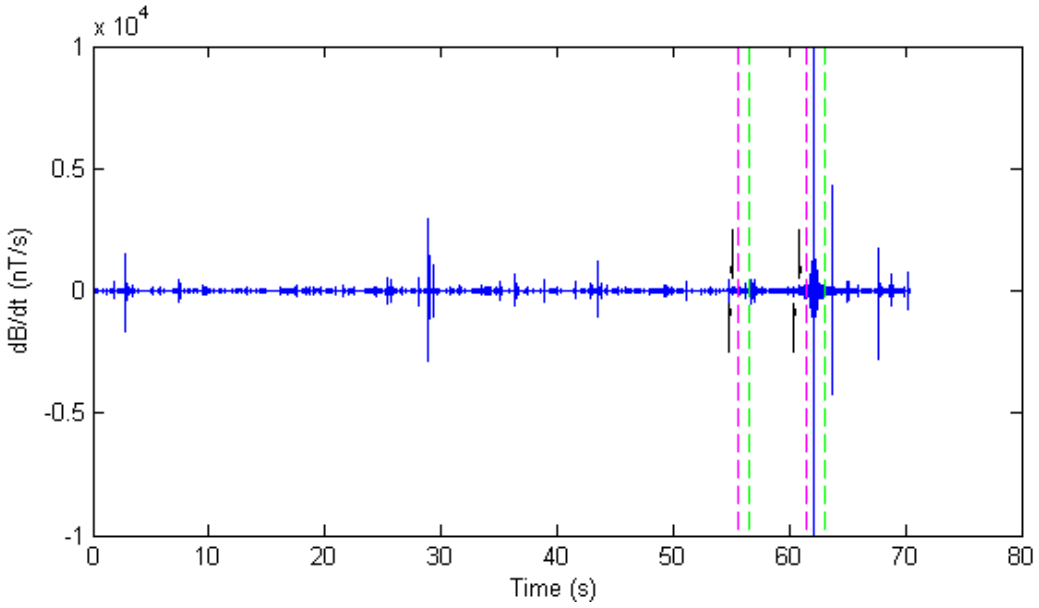

(f)

Figure 30. Relationship between signals of interest and audible cracking sounds for samples A3, (a), E3, (b) , E4, (c), F3, (d), G6, (e), and G7, (f). Magenta lines indicate the onset of audible cracking; green lines indicate their cessation. The final green line also indicates sample failure. Black arrows indicate signals as shown in Figure 20 appearing in the data. These signals are only apparent during or near audible fracturing. Thicker black arrows are due to regions with multiple signals occurring close to each other.

Appendix G: Marble Samples: F1, F2, F3, F4

Marble samples consistently behaved differently to other samples. The samples failed at far lower uniaxial pressures, and broke into larger, and fewer pieces than all other samples. Failures were far less violent, almost compliant, with minimal to no audible cracking, with pieces simply falling off rather than being violently ejected. The number of signals of interest varied from zero to nine. One explanation for the inconsistency may be the source of the marble. The marble was purchased from a carving store and was stored outside for a significant length of time before being purchased and cored. The depth and provenance of the sample are unknown. All other core samples were fresh and unweathered.

Samples F1 and F4 underwent axial failure, with neither containing any magnetic signals of interest prior to failure. Samples F2, and F3 underwent shear failure, and contained three and nine signals of interest respectively. The times of signals of interest for sample F3 are shown in Figure 30 (d). This is the only marble sample which exhibited magnetic signals for which a video and audio track was available. The magnetic profile for all samples is shown in Figure 31 (a) – (d) below. Only sample F4 exhibited a similar failure profile to what was seen in the non-marble samples (Figure 14 (b)). The second peaks at failure for samples F1, F2, and F3 all exhibit less sharp characteristics. This feature was not observed in the failure profiles of any other sample.

Samples of marble should be collected from a deep mining environment along with other sedimentary and metamorphic rocks to try and identify reasons for these variations in the results. These results indicate variations between rock types could potentially be significant.

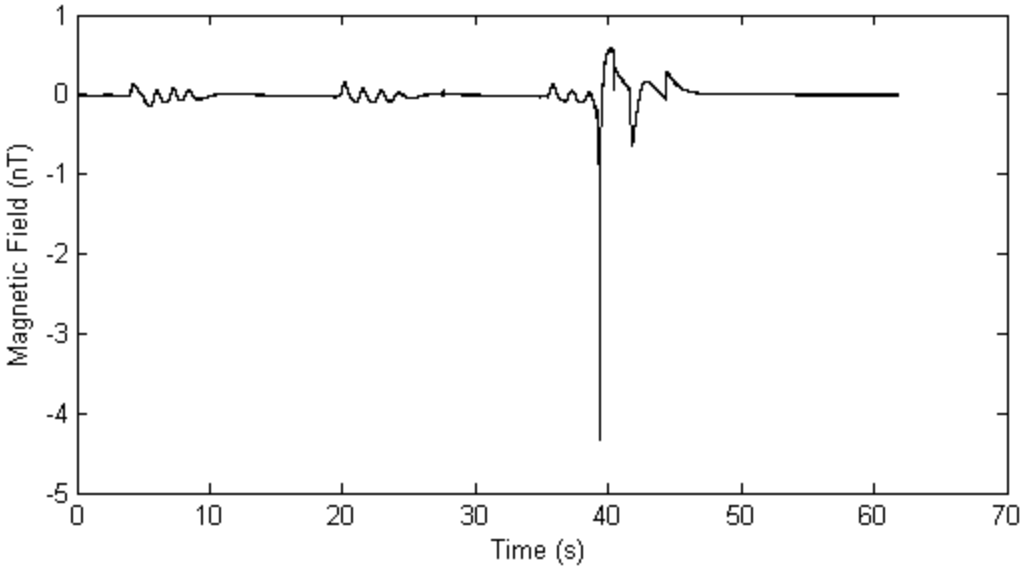
Magnetic Field (nT)
Time (s)
1
0
-1
-2
-3
-4
-5
0
10
20
30
40
50
60
70

(a)

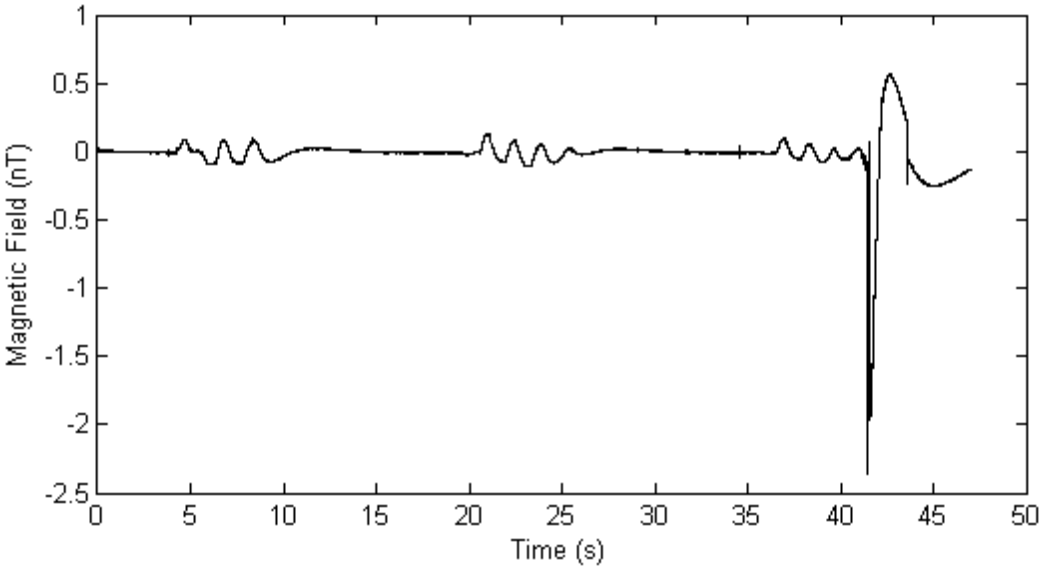
Magnetic Field (nT)
Time (s)
1
0.5
0
-0.5
-1
-1.5
-2
-2.5
0
5
10
15
20
25
30
35
40
45
50

(b)

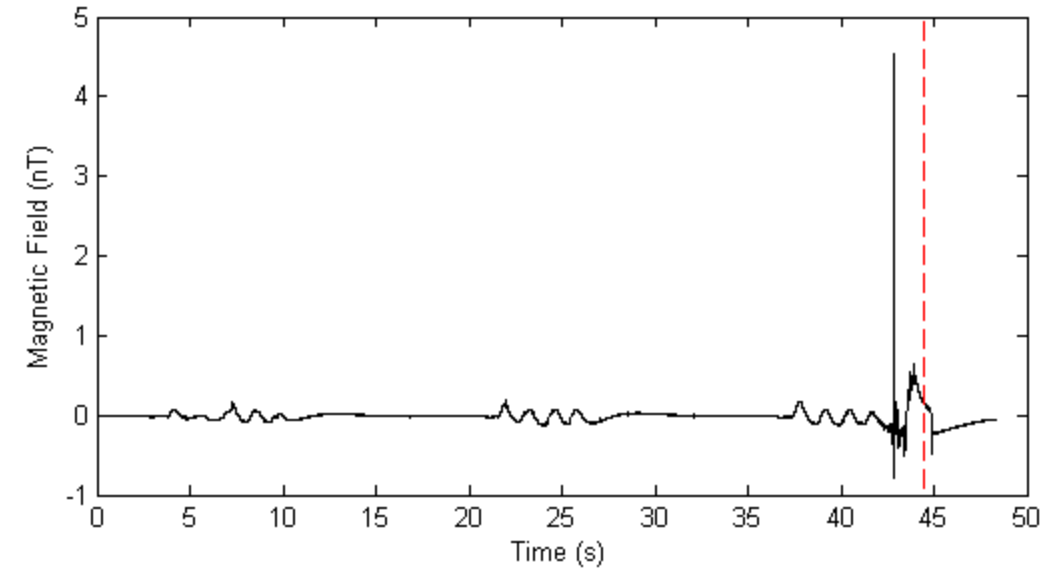

(c)

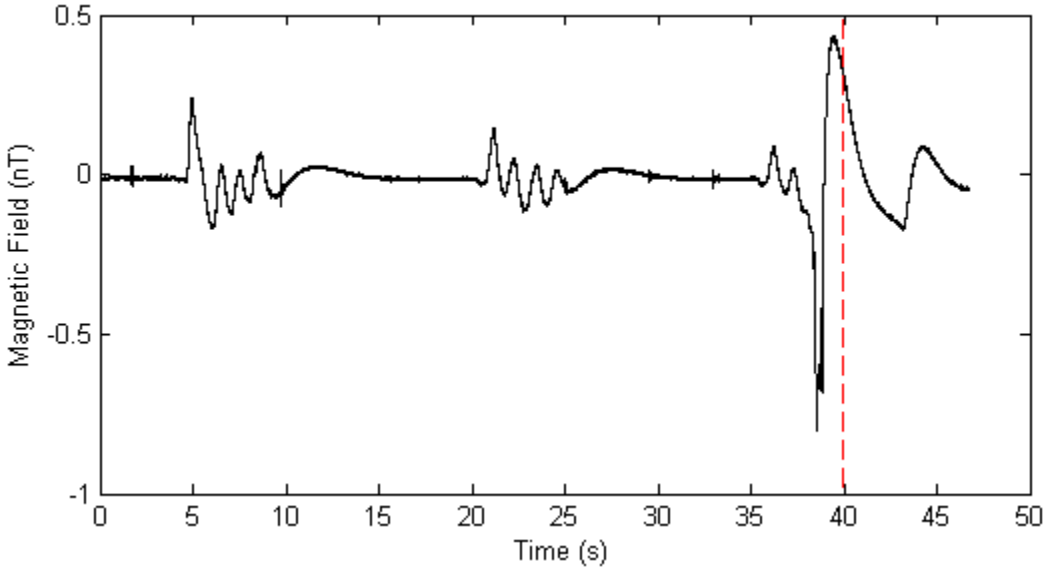

(d)

Figure 31. Four examples of magnetic datasets for marble samples. F1 (a), F2 (b), F3 (c), and F4 (d). Dashed red lines indicate failure for samples for which video recordings were available. Samples F1 (a), and F4 (d) underwent axial failure, with neither containing any magnetic signals of interest. Samples F2 (b), and F3 (c) underwent shear failure and contained three and nine signals of interest respectively. Locations of signals of interest for sample F3 are shown in Figure 30 (d). This is the only Marble sample which exhibited magnetic signals for which a

video and audio track was available. Only sample F4 (d) exhibited a similar failure profile to what was seen in the non-marble samples (Figure 14 (b)). The second peaks at failure for samples F1 (a), F2 (b), and F3 (c) all exhibit less sharp characteristics. This feature was not observed in the failure profiles of any other sample.

Appendix H: Correlation Graphs

For completeness, the correlation plots that do not show strong trends are shown in Figure 32 (a) – (f). These include correlations between the number of magnetic signals of interest or the difference between peaks (the amplitude difference between the negative peak and the positive peak at failure) and the other properties listed in Table 1 and Table 2. The correlations were made with 1) the total difference between peaks 2) axial compressive strength, 3) pressure at failure, 4) number of signals of interest, 5) plagioclase and alkali feldspar percentage, and 6) plagioclase, alkali feldspar and pyroxene percentage.

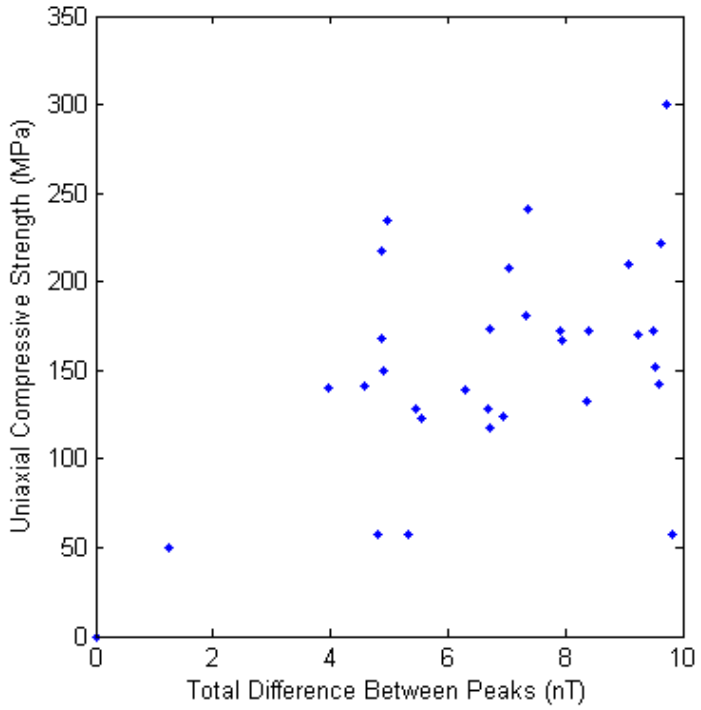

(a)

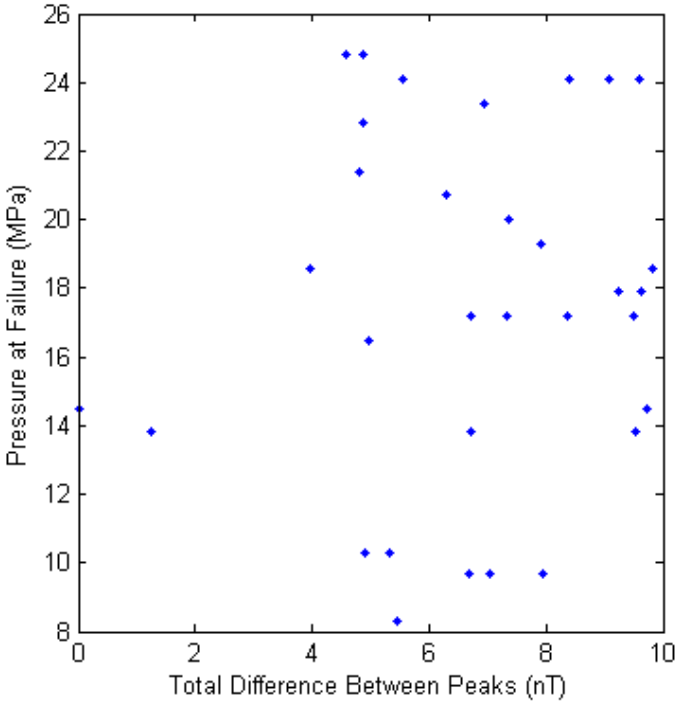
Pressure at Failure (MPa)
Total Difference Between Peaks (nT)
26
24
22
20
18
16
14
12
10
8
0
2
4
6
8
10

(b)

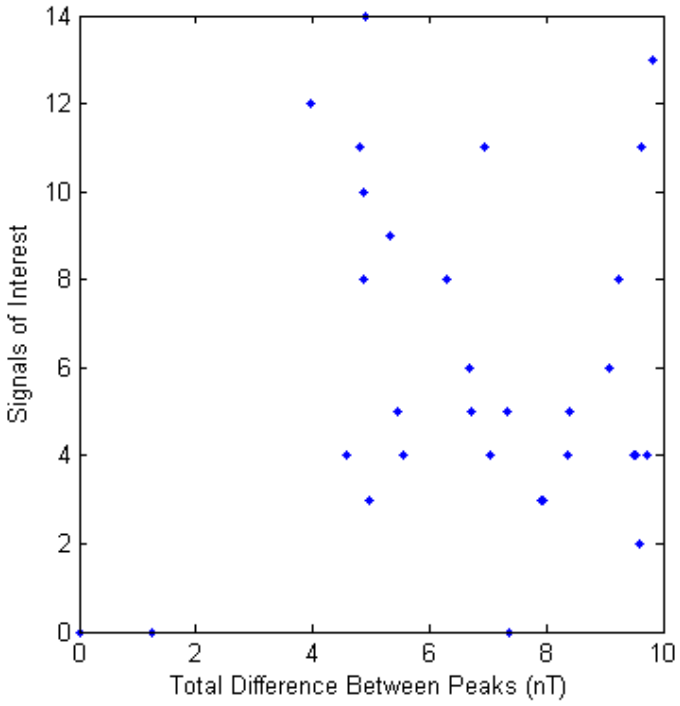
Signals of Interest
Total Difference Between Peaks (nT)
14
12
10
8
6
4
2
0
0
2
4
6
8
10

(c)

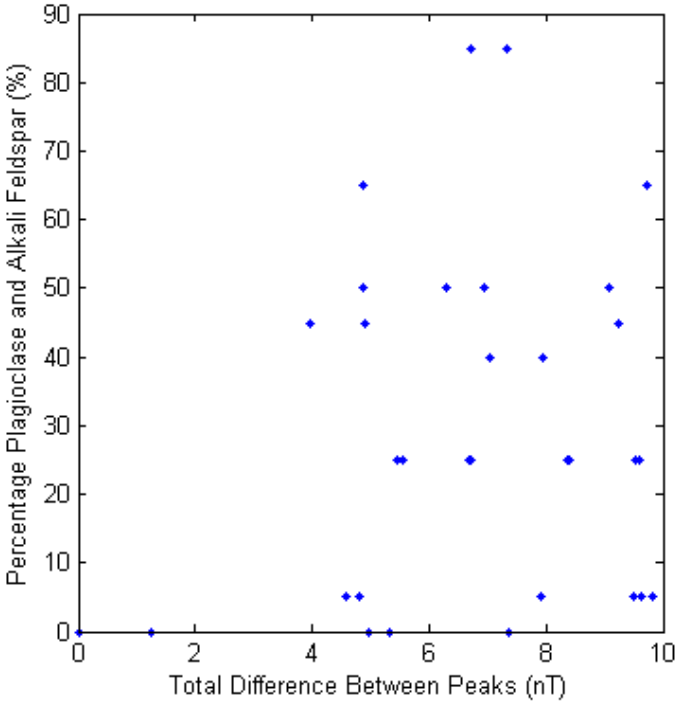
Percentage Plagioclase and Alkali Feldspar (%)
Total Difference Between Peaks (nT)
0
10
20
30
40
50
60
70
80
90
0
2
4
6
8
10

(d)

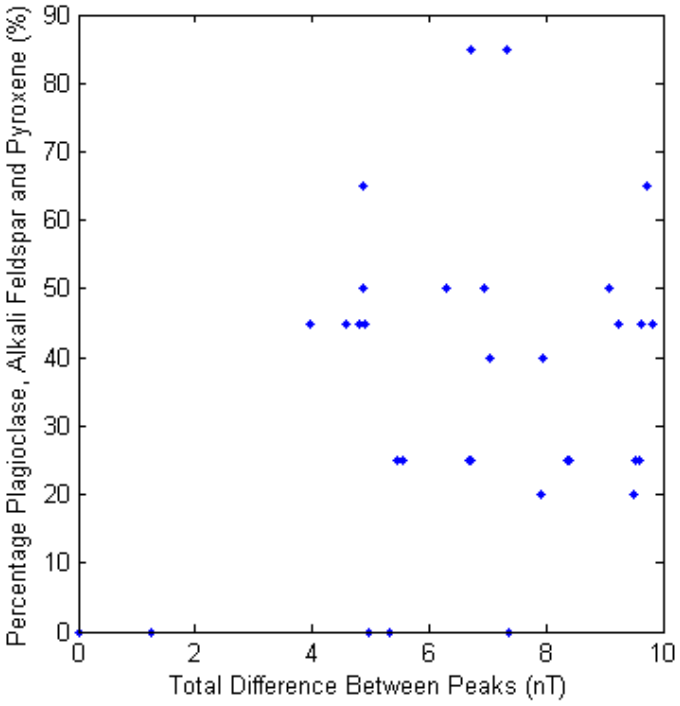
Percentage Plagioclase, Alkali Feldspar and Pyroxene (%)
Total Difference Between Peaks (nT)
0
10
20
30
40
50
60
70
80
90
0
2
4
6
8
10

(e)

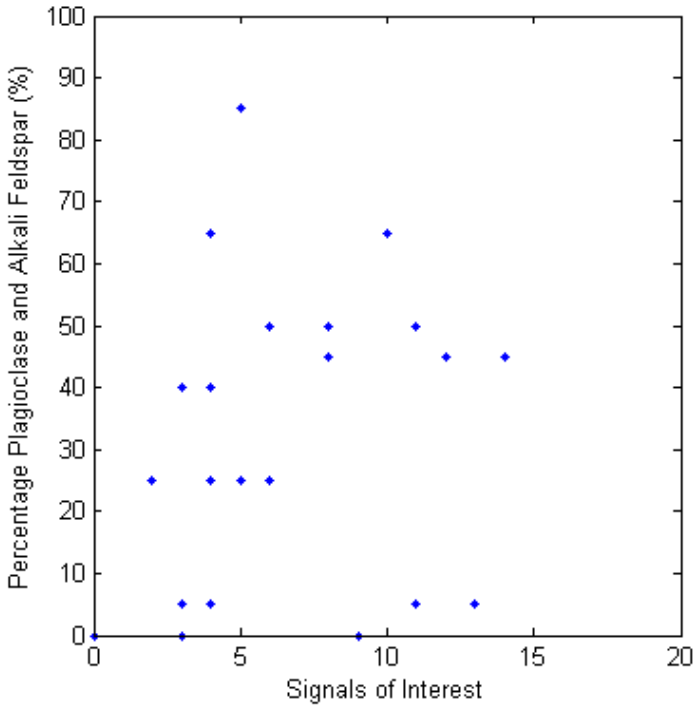

(f)

Figure 32. Correlation graphs of (a) total difference between peaks vs. axial compressive strength, (b) total difference between peaks vs. pressure at failure, (c) total difference between peaks vs. signals of interest, (d) total difference between peaks vs. plagioclase and alkali feldspar percentage, (e) total difference between peaks vs. plagioclase, alkali feldspar and pyroxene percentage, and (f) signals of interest vs. plagioclase and alkali feldspar percentage.